NORTHWESTERN UNIVERSITY

Solution Conformations of Graphene Oxide Sheets, and Two-Dimensional Nanofluidics

A DISSERTATION

SUBMITTED TO THE GRADUATE SCHOOL
IN PARTIAL FULFILLMENT OF THE REQUIREMENTS

for the degree

DOCTOR OF PHILOSOPHY

Field of Materials Science and Engineering

By

Andrew R. Koltonow

EVANSTON, ILLINOIS

December 2017

ABSTRACT

This work reports studies on the physical properties of collections of nanosheets. First, the configurations of graphene oxide sheets in solution are studied. Polarized optical microscopy reveals quickly and decisively that sheets remain flat and form lyotropic liquid crystals over a wide range of solvent conditions. When solvent conditions are inhospitable enough, sheets agglomerate into stacks rather crumpling upon themselves. Theory and simulation suggest that the crumpled state, which can be formed by compressing sheets, is metastable. This work might correct a persistent misunderstanding about the solution physics of graphene oxide. The other major area of study concerns the hydration layers in between lamellar stacks of exfoliated, restacked nanosheets. These layers comprise massive arrays of parallel two-dimensional nanofluidic channels, which exhibit enhanced unipolar ionic conductivity with counterions as the majority charge carriers. Based on the previously discovered graphene oxide nanofluidic platform, exfoliated vermiculite nanofluidic channels are constructed, which shuttle protons through the hydration channels by a Grotthuss mechanism, and which show superior thermal stability to graphene oxide. The 2D nanofluidics platform is also used to demonstrate “kirigami nanofluidics”, where ion transport can be manipulated by cutting the film into specific shapes. This can give rise to ionic current rectification. The rectification effect is attributed to the size and shape mismatch of the concentration polarization zones developed at the inlets and outlets of the nanofluidic channels. The kirigami nanofluidic platform can be used to fabricate ionic diodes and other simple devices. This material platform is expected to be a useful tool for nanofluidics researchers, because it offers a way to carry out nanofluidic experiments quickly with minimal equipment and little expense.

ACKNOWLEDGMENTS

My advisor, Prof. Jiaxing Huang, is a tireless churn of ideas, and simply keeping up has been an intellectual challenge of its own. He drills into students one central idea about how to communicate: Keep it crispy. Cut out all the details, ignore the higher order terms and the corrections, mine down to the core idea, then inspect that idea like you would a gem. He is relentless. He relishes the opportunity to talk about engineering, and especially to see what new ideas percolate back to him through the students. He is unusually dedicated to creating exceptional new classroom experiences, much to the teaching assistant's annoyance. He is an uncommonly dedicated mentor and I don't imagine I would have finished my dissertation without him. I've said too much. Keep it crispy.

My committee members are geniuses. The few times I've talked about my research with them, they have shown disarmingly powerful insight. For their time and valuable discussion, I am grateful to Profs. Monica Olvera de la Cruz, Yonggang Huang, and Cheng Sun. I would also like to thank Profs. Samuel Stupp and Erik Luijten, collaborators and former committee members who helped me formulate my qualifier proposal.

David Herman, Vincent Tung and Prof. Liam Palmer served as mentors to me at various times throughout my first few years. Without them I would have been clueless. I also want to thank the fantastic students and postdocs who have collaborated with me on research projects. In no particular order those people are Jiayan Luo, Adam Weingarten, Roman Kazantsev, Mark McClendon, Kalyan Raidongia, Hang Chen, Bernie Beckerman, Niels Boon, Taner Aytun, Xuan

Dou, and Jun Gao. Huang group members past and present are a great group and I am lucky to have them as friends and coworkers.

Countless friends, whom I need not individually embarrass here, have kept me going and helped me maintain a balanced perspective. When I see my friends' faces, I'm reminded how petty my research problems are. Natalie Estrada has shown continued love, patience, and support, which I return as best I can. I don't know where we will end up, but I am excited to find out together. My sister Elizabeth, whom I eventually learned to get along with, understands me like nobody else, and she will always be there for me as I will for her.

Nobody stands above my parents though. I didn't understand, at the time, how hard they were working to get me the best education possible. Education is never wasted. They poured all their energy into cultivating curiosity and kindness in us, encouraged us to chase down whatever hobbies interested us, and they never told us what we had to be apart from good. They take care of everyone else around them, and ask for nothing. I can't imagine better role models. Nobody else (except Liz) has the privilege of having Mary Schlaff and Sanford Koltonow for parents.

TABLE OF CONTENTS

LIST OF FIGURES

CHAPTER 1

INTRODUCTION

Ever since the isolation of graphene in 2004,[1] 2D materials have attracted intense research interest. Graphene's crystal lattice gives rise to a particular band structure that imparts exceptional properties, and for the first several years after its discovery, graphene was virtually the only 2D material of interest. Gradually, the field of 2D materials grew to include a wide variety of single-layer and few-layer sheet materials including insulators (*e.g.* boron nitride), semiconductors (*e.g.* metal dichalcogenides) and semimetallic graphene analogues (*e.g.* phosphorene and silicene). This family of materials is diverse in its chemistry, its synthesis methods, and its properties; however, several key properties are shared among the family. The ultra-thin sheets can easily be deformed out of plane, but are strong in-plane. To an extent, the mechanical strength can be understood in terms of Griffiths' century-old notion that atom-thin materials would be stronger than their bulk counterparts because of the absence of critical defects.[2-3] 2D materials also have the largest specific

surface areas among known materials (though an atomic wire would have an even larger area, if it existed). The large specific surface area makes 2D materials highly sensitive to their environment and imparts high double layer capacitance, making them appealing for a wide variety of sensors and energy devices.

The 2D material used for most of this work is graphene oxide. We will also use exfoliated vermiculite, which will be introduced at greater length when it comes up. Graphene oxide (GO) has been known for 150 years,[4] but was not widely pursued as a research topic until after the discovery of graphene. GO is a water-soluble single layer sheet produced by nonspecific chemical oxidation of graphite. A variety of oxidation methods exist, but most contemporary research (this work included) uses a variant of Hummers' method.[5] Upon reduction, GO is converted to reduced graphene oxide (rGO) a.k.a. chemically converted graphene (CCG), a highly defective form of graphene (Figure 1.1). While rGO/CCG has lower strength and conductivity than pristine graphene, the ease of GO processing is appealing for applications that can tolerate the more modest properties. GO dispersions can easily form redispersible cakes, aligned thin films,[6] and low-density hydrogels.[7-8] Research interest in GO has exploded in the last decade, and GO has been the subject of over 30,000 papers to date (per Web of Science). Most researchers studying GO are motivated by this material's relationship to graphene, its ability to convert into electrically conductive nanomaterial, and the manifold processing possibilities it enables.[9]

The work of Jiaxing Huang's group shows a noteworthy departure from this attitude, by considering graphene oxide as a novel material in its own right rather than as a disposable precursor to graphene.[10] A number of interesting properties and applications emerge from this line of thought. GO is a convenient experimental model of a 2-dimensional polymer, a trait Tanaka noted

as early as 1991 but did not pursue.[11-12] The expanded 2D morphology of GO implies that it will be well-suited to adhesive and composite filler applications.[13] The 2D polymer model also implies that new morphologies can be achieved by changing the shape of the flat sheet, imparting new properties without changing the surface chemistry. Additionally, the flexible sheet with a mix of hydrophobic sp^2 carbon patches and hydrophilic sp^3 carbon patches on its surface can act as a surfactant. Despite having a different structure than the conventional head-tail molecular surfactants, GO displays key characteristics of a surfactant including surface activity and the ability to disperse insoluble objects in solution. The Huang group has also developed processing methods that exploit these properties of GO to create new nanoparticles and nanocomposites.

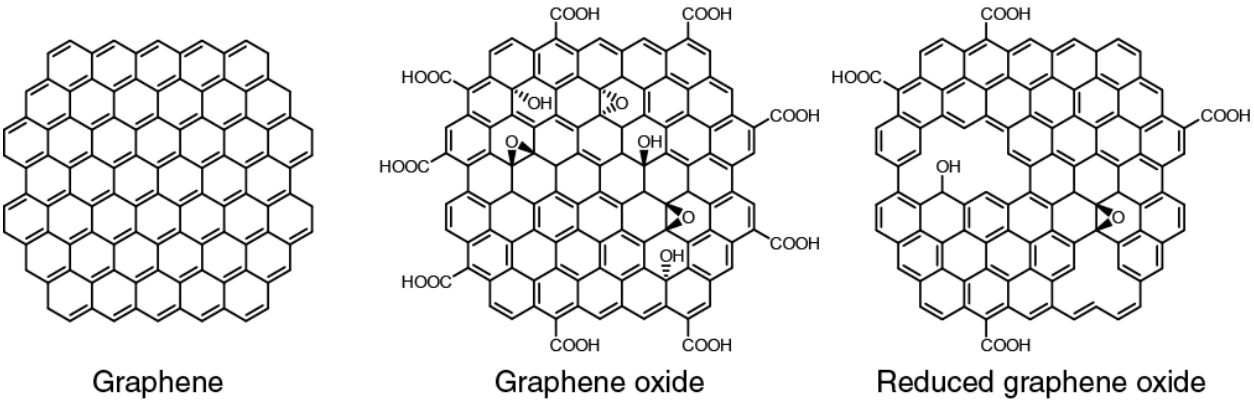

Figure 1.1. Representative chemical structures of graphene, GO, and rGO. *(left) Graphene consists of carbon atoms connected in a hexagonal pattern to form an atom-thick sheet. All carbons are sp^2 hybridized, and there is electronic delocalization across the sheet. (center) Oxidation and exfoliation of graphite yields graphene oxide. GO has the same connectivity as graphene, but many of the carbon atoms are oxidized, breaking the sheet-wide delocalization and rendering the sheet non-conductive. Small patches of conjugated sp^2 carbon can be found in some spots. Where the carbon is oxidized, various functional groups dangle off, including epoxides, hydroxides/phenols, and carboxylates. (right) Reduction and disproportionation reactions of graphene oxide produce reduced graphene oxide. In rGO, much of graphene's conjugation is restored, making the sheet conductive once again. However, the sheet is now highly defective – there are pinholes as well as lingering chemical moieties, which scatter current and impede the electrical performance compared to pristine graphene.*

Surfactants are widely employed as dispersing and emulsifying agents, and graphene oxide can serve these roles as well. Due to its size, GO acts as a colloidal surfactant capable of forming Pickering emulsions, where oil is stabilized in water through the formation of large, kinetically trapped micelles rather than the small, dynamic micelles formed by molecular surfactants.[14] GO is capable of dispersing large particles of hydrophobic material, and is particularly well suited for dispersing graphitic nanomaterials. Not only can GO disperse difficult nanomaterials and facilitate the formation of thin films, it can then be converted to rGO, embedding its payload in an electrically conductive matrix. This strategy was employed to create a solar cell with carbon nanotube composite active layers,[15-16] and might be used to create carbon-reinforced-carbon nanocomposites for mechanical, thermoelectric, and aeronautical applications.

The high surface activity of GO was also used to create Langmuir-Blodgett films, which allow for the deposition of monolayer GO films on a wide variety of surfaces, with a coating density that can be tuned continuously between isolated GO islands and contiguous films.[17] Further study found that the interaction between tightly packed sheets on a water surface could be controlled by tuning the hydrophilicity of the sheet edges. When sheets edges are relatively hydrophobic, sheets will be tightly pinned to the water surface, and two colliding sheets will crumple at their edges like continental tectonic plates. However, when sheet edges are more charged and more hydrophilic, then one sheet can dive beneath the other to create a smooth overlap at the edge.[18]

Crumpled GO balls (cGO) were formed by a novel aerosol method.[19] Crumpling requires significant deformation energies, which can be achieved by trapping the sheet in a shrinking sphere.[20] In the experimental realization, an aqueous dispersion of GO sheets was aerosolized to

form a mist of fine droplets, which were dried in an oven while suspended in air. As the aerosol dries, the GO sheets dispersed in the water are compressed by the retreating wall of the spherical droplet. The resulting cGO particle resembles a wadded-up sheet of paper. Since the GO sheets are surface active, they will tend to migrate to the drop surface early in the drying process, which may explain why cGO particles tend to resemble collapsed spherical shells (rather than other, non-spherical crumpled structures, *e.g.* accordions). However, surface activity is not strictly necessary for the formation of crumpled shapes.[20] The unusual shape of the cGO particle makes it resistant to aggregation, since the randomly wrinkled surfaces of particles cannot make intimate contacts with each other. Notably, this work offers us a physical manifestation of a crumpled-sheet morphology, a morphology that has been the subject of much theory and computational work, but is rarely seen in experiment. The relationship between cGO and the crumpled tethered membranes described in physics literature will be discussed further in chapter 2.

Some useful properties of GO emerge from large collections of sheets, rather than from individual sheets. For instance, GO sheets will spontaneously align with each other to form lyotropic liquid crystals.[21] Such behavior is a well-known property of anisotropic particles in solution, but the exceptionally high aspect ratio of GO sheets induces alignment of sheets at low concentrations. The lyotropic liquid crystals are nematic, with considerable overlapping area between sheets. Due to the large overlapping area, the aligned GO sheets form robust composite and xerogel fibers when dried,[21-22] and sturdy aligned aerogels when freeze-dried.[23] Nematic alignment is also found in air-dried and vacuum-filtered films of GO.

A GO solid of particular interest here is GO paper.[6] GO paper forms spontaneously as GO solution is dried against a flat surface. A simple way to make GO paper is by pouring GO solution

onto a non-stick plate or shallow dish, and letting it dry in air. The fabrication technique typically favored for GO paper, however, is vacuum filtration. Here, GO solution is pulled through a frit-supported flat filter membrane with pore size smaller than the GO sheets. Solvent and salt is pulled out through the nanoporous surface, while the larger sheets pile up. When dry, the stack of sheets formed this way can be peeled off the filter membrane as a free-standing film. Immense areal overlap between sheets holds the film together, so much so that the resulting GO paper can be stronger than the filter membrane on which it was made. The strength depends on the choice of filter membrane though. Anodized aluminum oxide filter membrane, widely used for GO filtration due to its superior flatness, was recently shown to release Al^{3+} ions into the feed solution during GO paper preparation. These polyvalent cations can crosslink stacks of polyanionic GO sheets, improving their yield strength and preventing them from being dissolved again. Meanwhile, GO paper made with inert membranes is more fragile, but can be dissolved again to form fresh GO solutions. The choice of filter membrane, long overlooked as trivial, was found to explain many discrepancies among previous studies of GO paper.[24]

One goal of my work is to assess how the Huang group's observations of GO can be made generalizable. Many of GO's properties, I expect, are simply determined by its size, shape, and charge density, without regard for specific chemical moieties. Another goal is to study the behaviors that emerge when sheets are considered in aggregate, rather than individually. As far as this work is concerned, the most important of these emergent properties is the formation of lyotropic liquid crystals with lamellar orientation. These two goals will be explored throughout the chapters to follow. In chapter 2, lyotropic liquid crystal formation will be used to examine the relationship between of GO and cGO, and the extent to which these materials can describe the

generic 2D tethered membrane model established in theoretical works. In chapter 3, we will see how lamellar stacks of GO sheets with large scale orientational order give rise to nanofluidic ion channels, and will discuss Raidongia's preliminary studies on this system. In chapters 4 and 5, we will generalize the nanofluidic model to a different 2D material, and determine the crucial material parameters that dictate how these devices work. In so doing, we also find that we can achieve nanofluidic ionic current rectification.

CHAPTER 2

CONFORMATIONS OF GRAPHENE OXIDE SHEETS IN SOLUTION

We are accustomed to picturing graphene oxide as a flat sheet, perhaps because of a bias built in to our observation methods. Whether by drop-casting, spin-coating, or Langmuir-Blodgett assembly[17]; by optical microscopy,[25] SEM, AFM, or fluorescence quenching microscopy (FQM)[26]; at daybreak, dusk, or dead of night; we almost always find ourselves looking at GO sheets that were laid flat on a favorable substrate before imaging (Figure 2.1a). Previous work in the Huang group, however, captured GO sheets in a crumpled-ball-like configuration (Figure 2.1b).[19] This was achieved by aerosolizing an aqueous dispersion of GO and drying it while it was suspended in air. Seeing that GO sheets dried in different geometries have different shapes, we consider the question: What is the preferred conformation of a sheet suspended in solution? Is a GO sheet an inherently crumpled object that gets flattened when it is dried against a flat substrate? Or, is it a flat object that gets crumpled when compressed in a shrinking solvent drop?

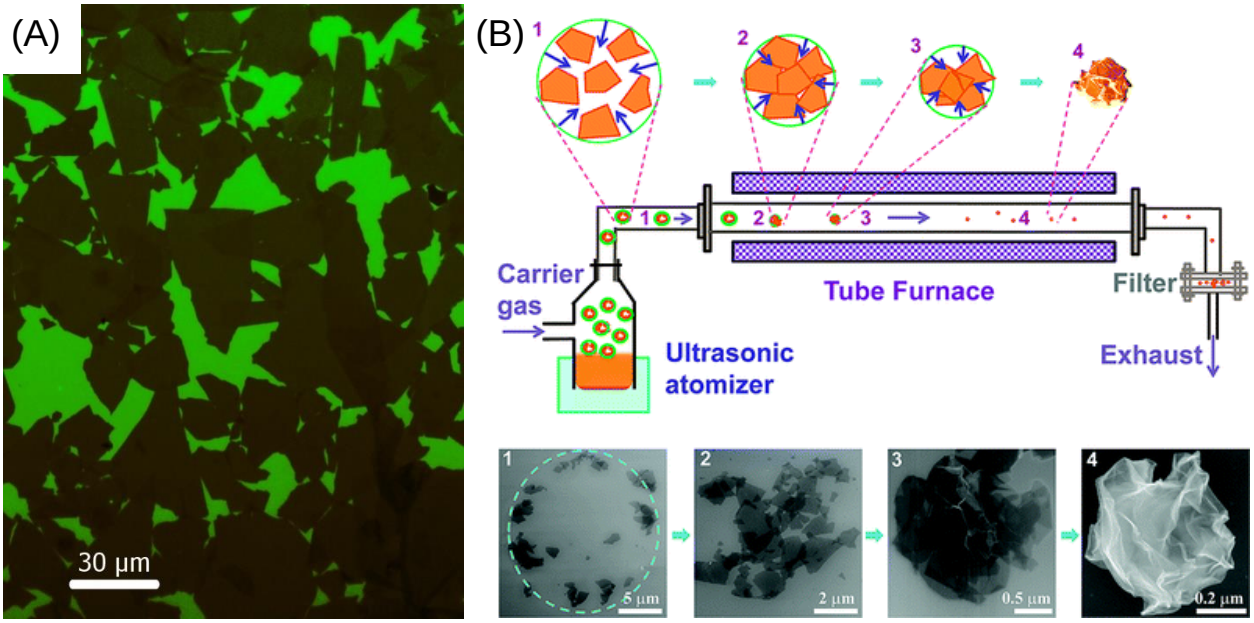

Figure 2.1. Flat versus crumpled states of GO. *(a) FQM micrograph of graphene oxide sheets, which were deposited on glass by Langmuir-Blodgett assembly. (b) Schematic illustration by Luo, depicting the synthesis of crumpled graphene oxide balls, reprinted with permission from J.Y. Luo et al, "Compression and Aggregation Resistant Particles of Crumpled Soft Sheets", ACS Nano, 5, 8943. Copyright 2011, American Chemical Society.*

The configuration of the sheet can have considerable ramifications on processing. Drying GO into *either* crumpled GO balls (cGO) or flat GO stacks will have irreversible effects on its properties and future processibility. Understanding the native configuration(s) of exfoliated sheets could have considerable ramifications for the development of processing techniques. Already numerous published papers, upon observing wrinkles in GO sheets, have incorrectly concluded that wrinkles are an intrinsic and inevitable consequence of solvent processing.[27-35] This is problematic because it cuts off lines of inquiry and discourages people from thinking of improved processing strategies. By clarifying this problem, we might prevent future misunderstandings of the sort. If our answer is generic enough, it can be of some use to people studying other exfoliated nanosheets, like MoS_2 or black phosphorus.

Decades earlier, polymer physics began seeking to understand how polymer chains occupy space, and in so doing set up a framework for describing the configurations of chains. Many 1-dimensional chains are adequately described by well-trodden analytic solutions. The simplest model, of an unconfined chain with no chain-chain or chain-solvent interaction, finds $R_G \propto N^{1/2}$ where N is the number of atoms in the chain backbone, and R_G, the radius of gyration, describes how much physical space the chain extends over. Equivalently we can say the scaling between N and R_G has a fractal dimension of 2, as the scaling relationship between N and R_G resembles that of a 2-dimensional object. This set of configurations maximizes the entropy of the ideal chain by placing it at the peak of a Gaussian distribution of potential configurations; elongating the chain decreases the number of configurations available, creating an entropic restoring force that resembles a spring. When favorable chain-solvent interactions are added to the ideal polymer, the polymer chain spreads out into more open configurations. Flory's model estimates the scaling of this configuration by seeking the energy minimum between the spring-like entropy and an enthalpic excluded-volume effect; it finds $R_G \propto N^{3/5}$, for a fractal dimension of 5/3. For a chain in hostile solvent, $R_G \propto N^{1/3}$, for a fractal dimension of 3. Derivations of these models and discussions of their shortcomings can be found in classroom textbooks.[36-38]

One might then ask, how does a 2-dimensional network of atoms occupy 3-dimensional space? Kantor and Nelson give a Flory-style approximation.[39] In their approximation, the entropic energy scales like KR_G^2 , while the self-repulsion energy scales as $\nu N^2/R_G^d$. N is the number of atoms in the sheet, R_G is the radius of gyration, K is the spring constant, ν represents the strength of self-repulsion, and d is the dimensionality of the space. Balancing entropy against self-repulsion in three-dimensional space they find the scaling relationship $N^2 \propto R_G^5$, giving the sheet a fractal

dimension of 2.5. However, their description of self-repulsion, adapted from the Flory model of a 1D polymer, is woefully insufficient to describe self-avoidance in a 2D network where any self-intersection of the membrane is strictly forbidden. Later works realized that self-avoidance lends bending rigidity and stifles large fluctuations. While most works attack the problem computationally, there has been progress in using renormalization methods to describe sheets.[40-42] Some later simulations found crumpled phases,[43-45] but most sufficiently large simulations have found that self-avoidance forces the sheets to stay flat, permitting thermal fluctuations and ripples on a small scale, but forbidding crumpling.[46-54] A recent review provides a helpful summary of the renormalization approach and history of thoughts on this subject.[55]

There are two experimental works that directly attempt to answer this question, and neither presents a complete picture. Tanaka used light scattering to study solutions of multilayer graphite oxide flakes,[12] which were around 10 atomic layers thick and microns in width.[11] Conventional TEM imaging found flakes with a flat appearance,[11] but scattering studies found $S(q) \sim q^{-2.5}$, implying that graphite oxide was crumpled in solution. Together, Tanaka's two papers on the subject found that this scaling law held across a two-decade **q** range. Furthermore, when acetone was added to create a poor-solvent condition, the fractal dimension steepened from 2.5 to 3.0, and this was interpreted as evidence that sheets collapsed into tight balls.[12] No TEM images were presented for the collapsed morphology. Tanaka did suggest an alternative explanation for this scaling law: that the flakes are flat but polydisperse with respect to thickness. However, he deems it unlikely that such a polydispersity would maintain such consistent scaling over two decades, and instead thinks it more likely that the flat sheets he sees in TEM are crumpled in solution and flattened during drying. In a follow-up work, Zasadzinski attempted to capture representative

solution configurations of graphite oxide sheets *via* freeze-fracture TEM.[56] Even with the drying effects eliminated, however, the sheets still appeared flat. Zasadzinski carried out a light scattering measurement of his own and found a fractal dimension of 2.15. In the two decades since then, no experimental work has reconciled Tanaka with Zasadzinski nor added new evidence to the debate.

It's worth noting, many respectable researchers of GO have misunderstood the body of work I've discussed so far in this chapter. In searching literature, I found 17 distinct examples of papers that make incorrect claims about the conformations of GO sheets and attribute those claims to Tanaka. A representative few are quoted in Table 2.1. I hope that by revisiting this old subject, I can prevent future errors of this sort.

Now, we have at our disposal something Tanaka and Zasadzinski never had: a positive control sample. Luo's aerosol synthesis method yields cGO particles that closely resemble crumpled paper balls. Whether cast from high-surface-tension or low-surface-tension solvents, and even under extreme pressure, cGO balls retain their shapes and resist aggregation.[57] It will be straightforward to compare solution properties of GO and cGO dispersions. We find that configurational differences between the two colloids can be revealed almost immediately, by looking for the presence or absence of liquid crystallinity in their dispersions.

The presence or absence of a birefringent liquid crystalline phase in solution is a simple qualitative marker of sheet conformation. Particles with high aspect ratio will spontaneously align to avoid jamming, increasing their net entropy by trading rotational freedom for translational freedom. The orientationally ordered phase is birefringent, meaning its refractive index is different

Table 2.1. Select examples of inappropriate conclusions taken from the findings of tethered membrane research.

Ref.	Quote
[62]	"Singular or plural aggregates of the thin-film particles are irregularly bent and deformed like crumpled paper. This shows that, when the affinity between the particles and the dispersion medium is very low…particles shrink by entropy elasticity like linear flexible macromolecules, and the amount of dispersion medium which is held among many particles decreases."
[63]	"The spin-coating process … leads to stretching and flattening of graphene oxide sheets that might be to some degree crumpled / wrinkled in the colloidal suspension. For example, light-scattering studies of colloidal suspensions of graphite oxide have been analyzed to yield a fractal dimension of 2.54 ± 0.05 (where 2.0 is for a completely flat membrane and 3.0 is highly crumpled and thus compact). Further study of how the sheets end up being so flat in the spun-cast films is indicated."
[64]	"Another possible contribution to this roughness [in an AFM image of graphene sheets] may be the crumpling of graphene sheets"
[17]	"Prior studies showed that GO tends to collapse and adopt three-dimensional compact conformations in 'poor', less polar solvents such as acetone. There, we chose the simplest polar protic alcohol—methanol—as the spreading solvent."
[27]	"Corrugation and scrolling are part of the intrinsic nature of graphene nanosheets, which result from the fact that the 2D membrane structure becomes thermodynamically stable via bending"
[65]	"As with a coiled polymer, the level of membrane corrugation is determined by the competition between the steric constrains and configurational entropy. If the intra-membrane affinity is increased, the membrane may collapse to a compact conformation; while under appropriate circumstances, the membranes can also be 'flattened' … When acetone is added into an aqueous solution of graphite oxide, the flakes tend to take a compact spherical morphology in order to match the polarity shift of solvent and minimize free energy."
[28]	"In the present case, TEM clearly shows that GO sheets are full of wrinkles and foldings. Therefore, in the colloidal state, GO sheets are not expected to be extended and flat, but GO possibly (certainly from our point of view) forms smaller folded colloidal entities, which in turn may give rise to smaller equivalent hydrodynamic radii detected by DLS…In support of our findings, previously reported results also point to similar conclusions regarding the folded (crumpled) configuration of GO colloids."
[66]	"[TEM images] show that the sheets of graphene are crumpled and the edges are folded. It has been reported that the morphology of GO can be affected by the solvent. In our cases, during drying, with ethanol evaporation, the GO-T flakes tend to crumple to minimize the surface energy."

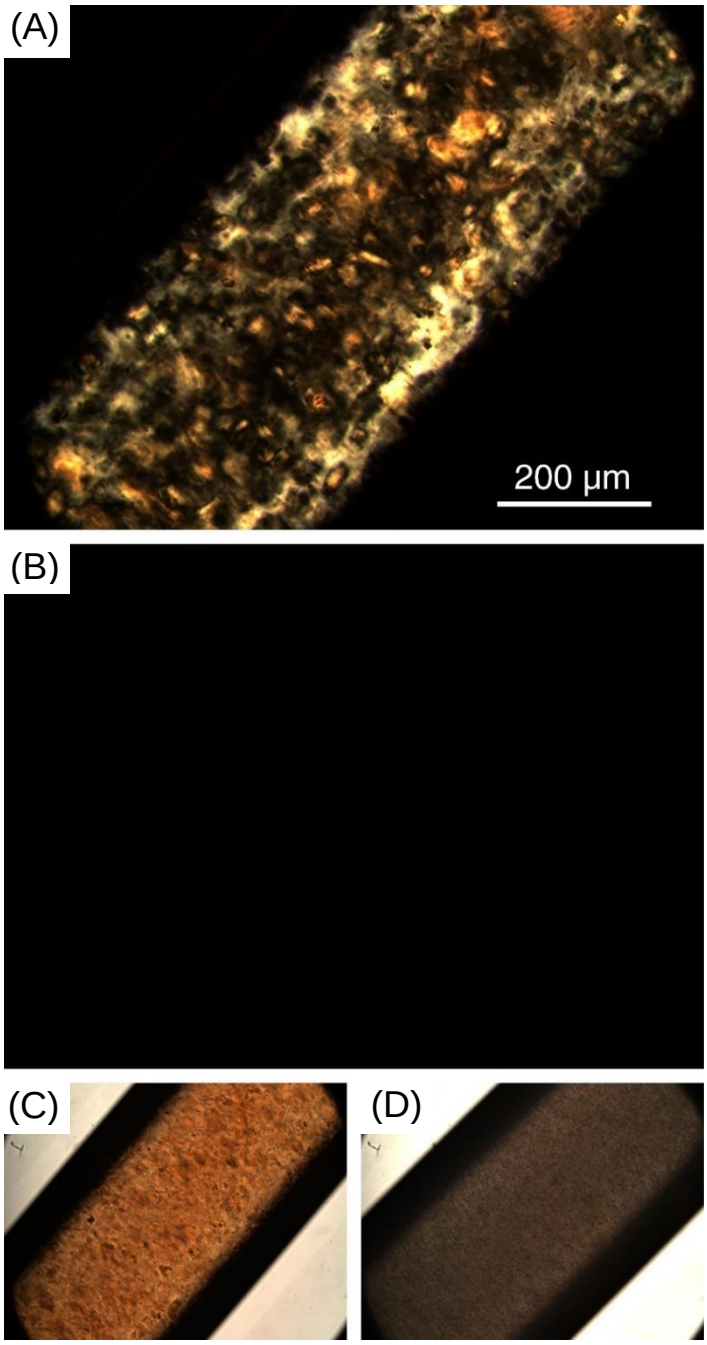

Figure 2.2. GO solution is a birefringent liquid crystal, and cGO solution is not. *Aqueous dispersions of GO (a, c) and cGO (b, d) in glass capillaries are imaged by polarized (a, b) and non-polarized (c, d) transmission light microscopy. (a) GO passes light between crossed polarizers, indicating that it is birefringent and therefore liquid crystalline. Sheets appear to be grouped into liquid crystalline domains of around 10–100 µm. (b) No such birefringence is seen from cGO. The bright field images of (c) GO and (d) cGO dispersions show that the cGO dispersion is slightly less transparent. This is because the cGO dispersion was prepared at a higher concentration (3 vs 1 mg/mL), to make liquid crystal formation more favorable for the cGO.*

for different polarization angles of light. When Onsager first derived the conditions for the isotropic-to-liquid-crystalline phase transition, he cautioned that the second-order virial approximation used in the derivation could not give quantitative results for 2D particles,[58] and while later calculations made progress on extending the result to 2D particles,[59-61] we should still take a qualitative view of liquid crystal formation for our samples. Calculating the exact phase behavior will be nearly impossible in our case, since the GO sheets are polydisperse, irregularly-shaped, and flexible. It's safe to say, though, that particles which form a liquid crystal phase are higher in aspect ratio than those that don't. By looking for birefringence in a solution of colloids, we can quickly identify whether a liquid crystal phase is present; and, though intermediate aspect ratios will not necessarily form liquid crystals, we can at least distinguish between isotropic conformations and high-aspect-ratio conformations.

Fortunately, this is enough. GO sheets can readily form a liquid crystalline phase.[21, 67-68] The birefringence of a GO solution can be seen by polarized light photography/microscopy (Figure 2.2a). Indeed, the nematic phase has been observed in GO solutions, at a concentration threshold that roughly agrees with Onsager's prediction.[59] A GO sheet crumpled into a ball is essentially isotropic, with aspect ratio near 1. For crumpled graphene balls, no nematic phase is observed no matter how high the solution concentration is (Figure 2.1b). These observations show that liquid crystallinity is a sufficient marker for the conformational difference between GO and cGO.

We then reproduce and extend Tanaka's "poor solvent" conditions. As shown in Figure 2.3b, GO remains liquid crystalline when dispersed in a series of worsening solvents. Furthermore, as shown in Figure 2.3c, when GO dispersed in poor solvent is given time to settle, it settles into a birefringent phase. At >70% acetone, the solvent condition is poor enough to induce aggregation

of GO sheets. In this case, GO forms a loose birefringent gel at the bottom of the tube. If GO crumpled into a ball under poor solvent conditions, as previous work suggests it should, then it should lose its ordering and its birefringence. Indeed, dispersions of crumpled balls (Figure 2.3d-e) appear dark between crossed polarizers (Figure 2.3f). It appears that when solvent conditions become bad, GO sheets prefer to aggregate with each other rather than folding upon themselves.

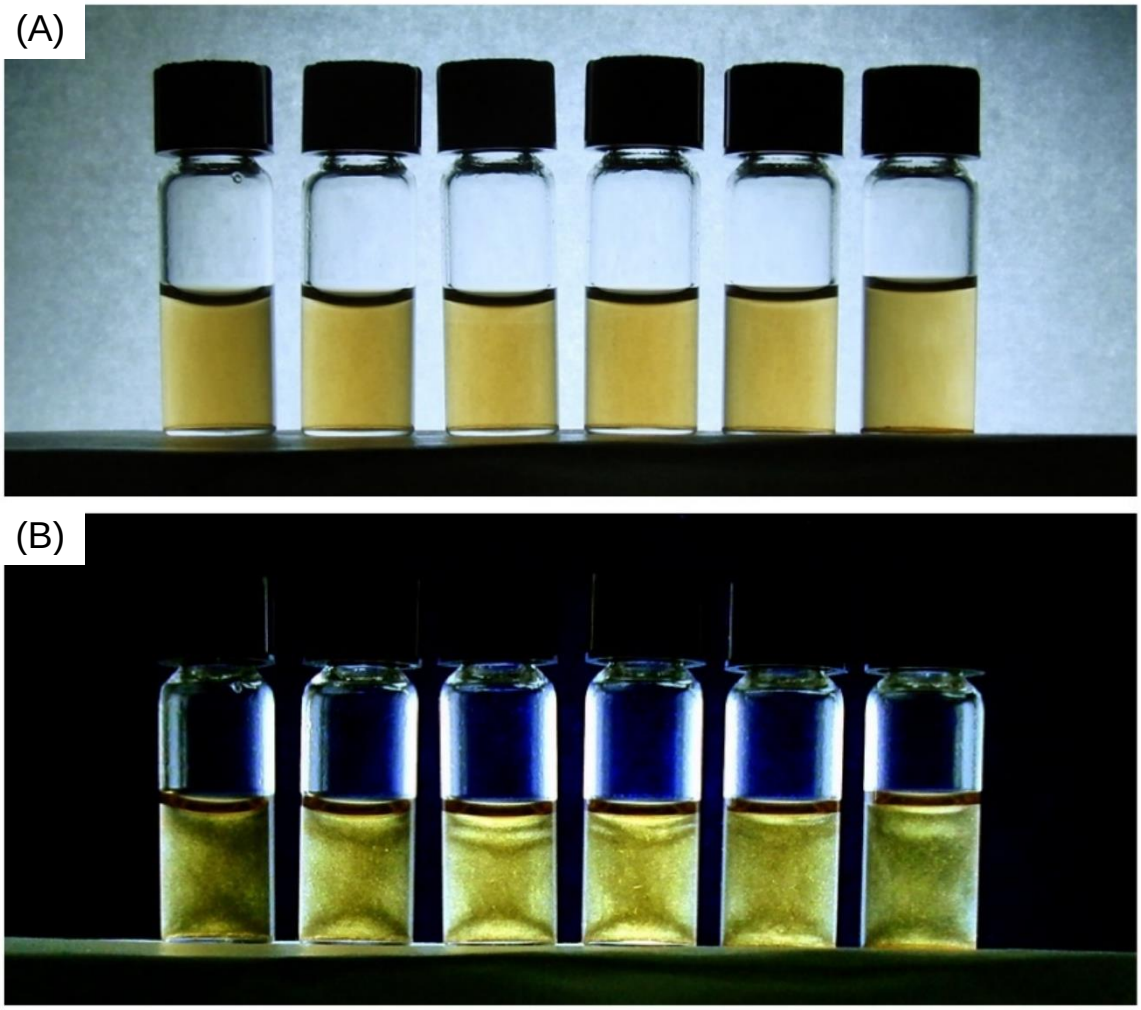

Figure 2.3. GO is liquid crystalline across various solvent conditions. *(a) Unpolarized and (b) Crossed-polarizers transmission photograph of freshly-mixed GO dispersions at 0.1 mg/mL in acetone/water mixtures of (from right to left) 0/100, 10/90, 30/70, 50/50, 70/30, and 90/10 vol%. GO dispersion is birefringent at all solvent conditions.*

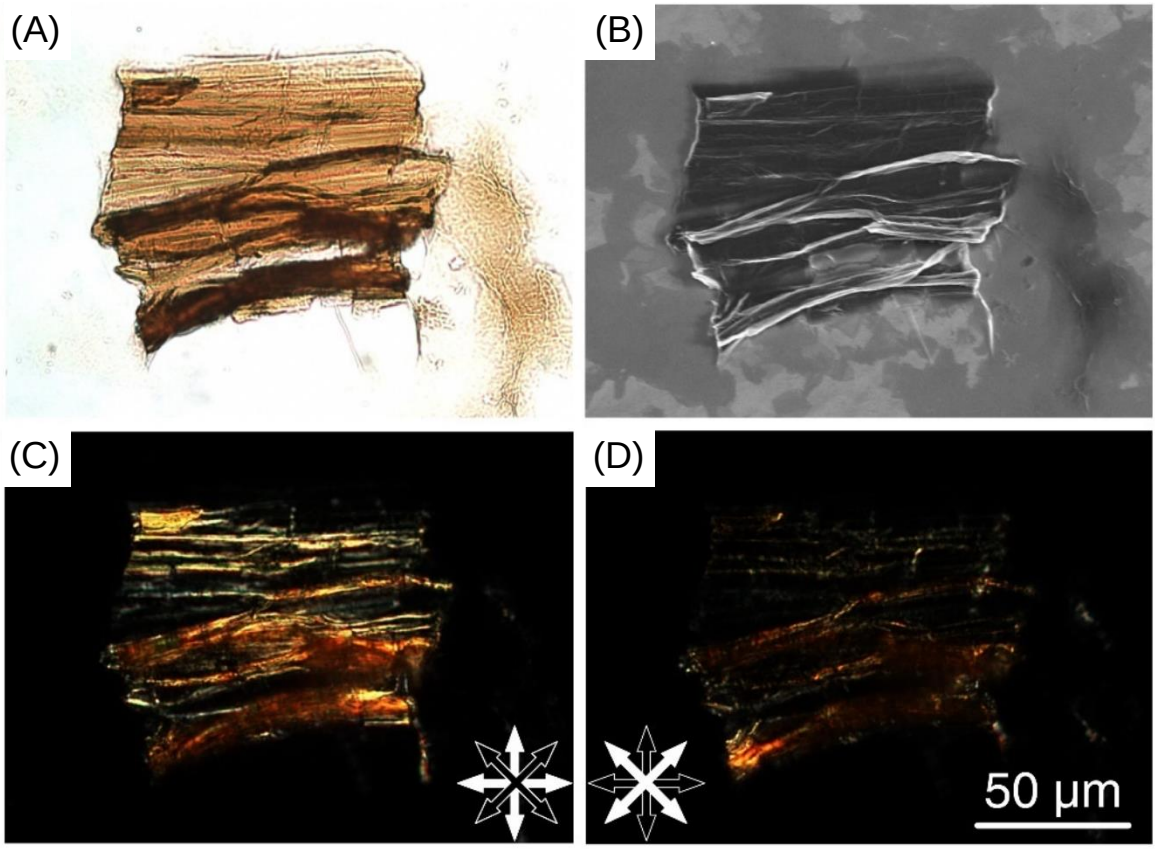

Figure 2.4. GO aggregate precipitated out of solution retains flat morphology and orientational order. *(a) Transmission optical microscopy and (b) SEM of an aggregate reveal striation with the appearance of oriented flakes. (c, d) Polarized optical microscopy reveals birefringence. Horizontally-aligned striations (c) appear at polarizer angles of ±45°, and (d) are dark at polarizer angles of 0°/90°, indicating that the apparent alignment of the visible striations matches the optical axis of birefringence.*

One possibility our evidence has not yet ruled out is that the confining influence of neighboring sheets prevented a crumpling transition, and crumpling would have been favored were sheets subjected to bad solvent in isolation. To show that this is not the case and crumpling really is unfavorable, we study sheets at dilute concentrations, below the threshold concentration for formation of the nematic phase. Aqueous solutions are diluted to 0.01 mg/mL, then dropped in 10 µL aliquots into a 100 mL acetone bath, so that GO sheets are isolated when they are exposed to poor solvent conditions. Addition continues until the bath composition is 25% water (and therefore

25 ppm GO by weight). GO aggregates are seen in this sample. When some of this aggregated GO is pulled out and viewed under the microscope, it still appears as a birefringent aggregate of many sheets. SEM and light microscopies show that the aggregate contains aligned flat flakes, whose alignment corresponds to the axis of birefringence (Figure 2.4). Furthermore, if we swirl the acetone bath to briefly disperse the particles, we see optical schlieren, small birefringent "clouds" with varying optical axis orientations, revealing that the particles redispersed this way are locally aligned (Figure 2.5). These observations confirm that individual GO sheets stayed flat long enough to traverse the acetone and restack with each other.

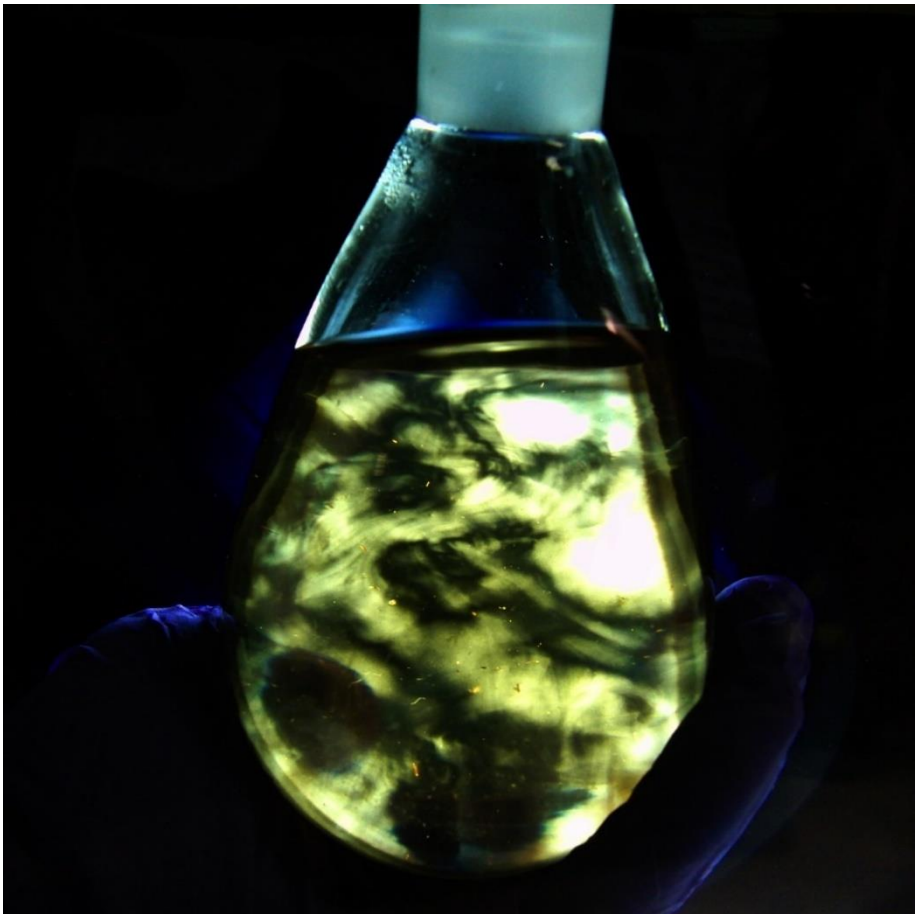

Figure 2.5. Optical schlieren are observed from dilute GO in a large acetone bath. *GO sheets precipitated to the bottom of the bath, but could be briefly redispersed by swirling. When this solution is photographed between crossed polarizers, light and dark bands are seen, indicating the presence of orientationally-ordered domains.*

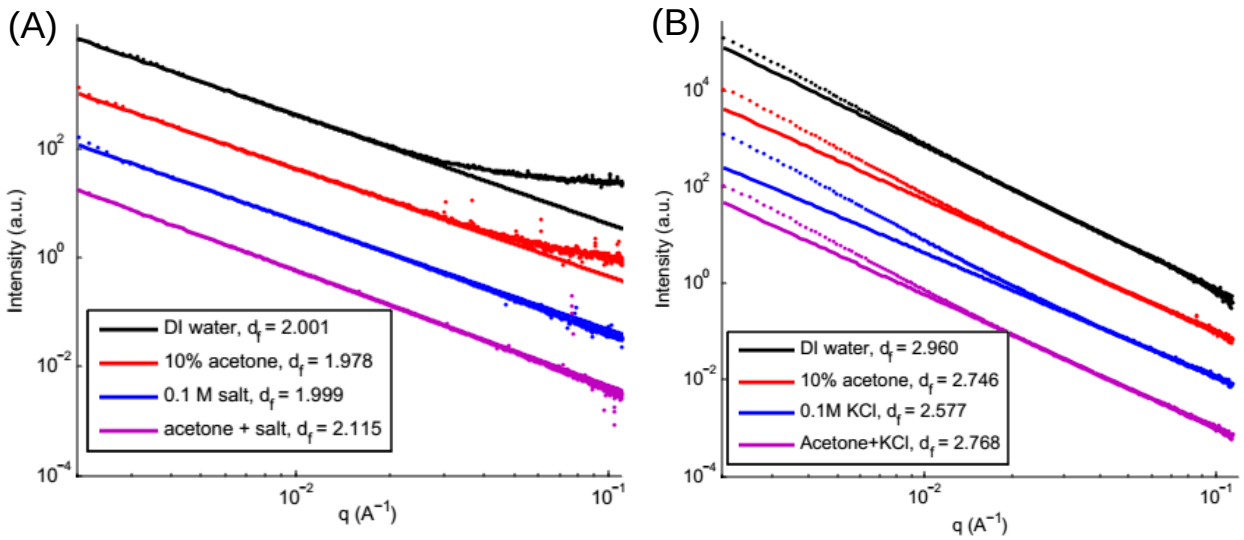

Figure 2.6. Small angle X-ray scattering shows that GO and cGO have different scaling behaviors. *(a) Scattering traces from GO are well-fit by a power law with fractal dimension 2. (b) cGO may be multifractal, with fractal dimension near 3.0 at low* ***q****, and dimension between 2.5-3.0 at higher* ***q****. Further SAXS studies may reveal more information about the texture of cGO balls.*

Small-angle X-ray scattering (SAXS) was carried out to see if the fractal dimensions of GO and cGO samples could be found. Samples of each colloid were prepared in deionized water, and salt and/or acetone were added to create a self-attractive solvent condition. Scattering data was averaged over all orientations, and for each sample a solvent blank was measured and subtracted from the sample data. Data for GO sheets were then fit by a least-squares method over the wavelength range 20 $\mu m^{-1} < \mathbf{q} < 200\ \mu m^{-1}$, corresponding to correlations on the 5 – 50 nm length scale. As seen in Figure 2.6a, GO sheets have fractal dimension of almost exactly 2 in water, 0.1 M KCl solution, and 10 vol% acetone in water. When salt and acetone were added together, the fractal dimension increased to 2.12, likely due to aggregation. Meanwhile, cGO had a much higher fractal dimension. cGO was found to be multifractal, with a scaling exponent of around 3 on the >50 nm length scale, and a slightly smaller scaling exponent on the shorter length scale. The short-

length-scale exponents range from 2.56 to 2.96, as shown in Figure 2.6b. The multifractal behavior suggests that the crumples maintain their overall shape across all solvent conditions, while experiencing minor changes in stiffness or wrinkling on a nanoscopic level. Surprisingly, the crumple was most "expanded" in the salt condition, even though salt is known to aggregate GO sheets. Further study of this system might in fact reveal short-length-scale morphological transitions. However, the crumple does not change its overall shape under any condition.

By now it's becoming clear that both configurations are metastable, and GO will not spontaneously switch between the two configurations in solution. Therefore, to switch from one configuration to the other, GO must overcome an energy barrier that far exceeds thermal fluctuation. Note, even if one configuration is massively thermodynamically favored, the sheets can still be kinetically trapped in the other configuration. The only way to switch the configuration, then, is by applying considerable external force.[69]

This interpretation is further supported by the work of Beckerman and Luijten, who carried out Langevin metadynamics simulations. A single charged sheet in implicit solvent was initialized in a flat configuration and allowed to equilibrate. Then, that configuration was outlawed and the sheet sought out the next most favorable configuration, which in turn was outlawed. By iterating in this manner and calculating the relative energy of each configuration, the sheet was forced to fold or collapse in whatever way it deemed least costly, and the energy barrier to that fold was traced out. The least costly maneuver was found to be a single lengthwise fold, and at room temperature the barrier to that fold is 250 kT. Such a sheet will almost certainly not spontaneously fold during the lifetime of our universe. The barrier to crumpling is probably considerably higher than the barrier to formation of a single fold.

A puzzle remains. The work of Tanaka clearly shows a fractal dimension of 2.5 for GO in water, and 3.0 in bad solvent (10% acetone). How do we account for this difference between Tanaka's product and our own? First, consider that the products were physically different in a crucial way. Tanaka's GO synthesis method produced multilayer GO flakes. As Tanaka noted, polydispersity in the flake thickness could increase the observed fractal dimension for a dispersion of flat flakes. A related idea was explored at greater length by Abraham and Goulian, who calculated structure factors for simulated 2D membranes. They found that when the structure factor was averaged over all orientations, as Tanaka's is, then even a flat membrane can scatter with a scaling exponent of 2.5 when there is nontrivial scaling in thickness.[70] Abraham and Goulian find that entropy-driven fluctuations out of the plane of the membrane can produce such thickness scaling, but polydispersity in the flake thickness would have the same effect. The formation of small aggregates could contribute to the fractal dimension as well.[71] Tanaka's GO flakes were noted to precipitate out when only 10% acetone was added. Meanwhile, our contemporary GO product stayed dispersed up to 70% acetone, and when it did precipitate, it did so as a gel. Secondly, we note that our scattering experiment (SAXS) sampled a different length scale than Tanaka's (DLS), and there is precedent for 2D membranes showing different scaling dimensions at different length scales.[72] SAXS is the more relevant technique since it captures a length scale in between the lateral dimension of GO sheets (~1-10 μm) and the expected persistence length of the sp^3 carbon lattice of GO (~1-10 nm). Meanwhile, Tanaka's longer-wavelength scattering experiment is likely to have captured inter-sheet correlations. For these reasons, when our result differs from Tanaka's, ours better represents the properties of individual GO sheets.

In conclusion, individual GO sheets do not take on crumpled configurations in solution. Under the conditions most commonly used for processing GO, they exist as extended flat sheets. When self-attractive forces are stronger, the sheets prefer to restack or fold flat, forming anisotropic platelets. However, crumpled conformations can be formed by applying an isotropic confining force.

Methods

Graphene oxide sheets were prepared by a modified Hummers' method[73] and were dispersed into a 2 mg/mL aqueous stock prior to mixing and diluting with water and acetone. Graphene oxide crumpled balls were prepared from graphene oxide sheets by Luo's previously-published procedure,[19] using a furnace temperature of 150°C. SAXS samples were measured via synchrotron radiation in quartz capillaries at a concentration of 0.1 mg/mL. SAXS data were orientationally averaged, then background subtracted with a solvent blank, prior to least-squares fitting.

CHAPTER 3

GRAPHENE OXIDE AS A TWO-DIMENSIONAL NANOFLUIDIC MEMBRANE

Nanofluidics, broadly defined, is the study of the ways liquid properties can be affected and/or controlled by nanoscale confinement.[74] Liquid properties can differ dramatically from bulk if the physical characteristic length scales underpinning those properties (such as Debye length, slip length, and hydrodynamic radius) are similar to the length scale of the confinement. Research areas within the purview of nanofluidics include confined water dynamics and transport,[75] confined polymer physics,[76] separation of polyelectrolyte chains (via size- or charge-dependent mobility differences)[77] and ions (via charge or outright size-exclusion)[78], as well as studies of ion

transport.[79-83] This work will only concern itself with ion transport, but in chapter 6 we will discuss other possible applications of our nanofluidics platform.

Electrolytes confined in nanochannels exhibit different properties than in bulk. For example, when electric field is applied to a bulk salt solution, cations and anions simultaneously move in opposite directions to generate ionic current. This symmetry is broken, however, at charged solid walls. The charged walls repel co-ions (ions whose charge is the same sign as that of the wall) and attract counterions (ions whose charge is opposite in sign). The region over which this charge imbalance exists is known as a *diffuse electric double layer*, and its characteristic thickness is the Debye length, κ^{-1}. The Debye length is a property of the solution, and is unaffected by the charge, potential, or composition of the surface. For an arbitrary electrolyte solution, the Debye length is:

$$\kappa^{-1} = \left(\sum_i \frac{\rho_{\infty i} e^2 z_i^2}{\varepsilon_0 \varepsilon k T} \right)^{-\frac{1}{2}}$$

where ρ_∞ and z are the concentration and charge of each ionized species in the solution. Hereafter we will usually be considering a monovalent salt solution of concentration c in water at 25°C, in which case we can simplify the above equation to:

$$\kappa^{-1} = c^{-\frac{1}{2}} * 0.304 \text{ nm } \sqrt{M}$$

When two charged walls are so close together that they intrude into each other's diffuse electric double layers, then the electrolyte will experience charge imbalance all throughout the channel between those walls. In some cases, the co-ion can be completely excluded from the

channel. The exclusion of the co-ion does not violate the principle of electroneutrality – every excess positive ion within the nanochannel is balanced by a negative charge on the channel wall (or vice versa). However, such exclusion can give rise to unusual ion transport properties such as unipolar ionic transport and enhanced ionic conductivity. To access and exploit these properties, one must create nanofluidic channels that are stably charged and sufficiently narrow.

A common feature of nanofluidic ion channels is the existence of two distinct regimes in the relationship between ion concentration and conductivity. Consider a channel that is of a thin, broad rectangular prism shape. For each net charge on the nanochannel wall, there is an associated counterion inside the channel, which contributes a concentration-independent term to the ionic conductance according to:

$$G_{sc} = 2\mu_+\sigma_s(w/l)$$

where μ_+ is the ion mobility, σ_s is the surface charge density, and w and l are the width and length of the channel. At the same time, the bulk electrolyte contributes additional current carriers to the nanochannel, particularly at the high concentrations where Debye length is short. The bulk contribution to conductance is linearly dependent on concentration, taking the form:

$$G_b = qN_a\frac{wh_0}{l}\sum_i \mu_i C_i Z_i$$

where q is the elementary charge, N_a Avogadro's number, h_0 the height of an individual channel, and μ, C, and Z are the mobility, concentration, and charges of the ions in the system. The conductance of the system is approximately the sum of these two contributions. For a simple binary electrolyte, the total system conductance takes the form:

$$G_0 = 2\mu_+\sigma_s\left(\frac{w}{l}\right) + q(\mu_+ + \mu_-)C_bN_a\frac{wh_0}{l}$$

where C_b is the bulk salt concentration. In the high concentration limit, the bulk term dominates. Conductivity will scale linearly with concentration as it does for bulk solution, and the influence of the nanochannels' surface charge is minimal. Anions and cations alike are flowing through the nanochannels, mostly unimpeded by surface charge or confinement. At the low concentration limit, the bulk term falls away as the surface charge term dominates. Here, the concentration of charge carriers inside the channel is dictated by the amount of excess charge on the channel walls, and exceeds the concentration of the bulk reservoir. The carrier density inside the channels, and thus the conductivity as well, is independent of the exterior electrolyte concentration. In a plot of concentration vs conductivity, there are two distinct regimes, a bulk regime and a surface-charge-governed regime. The surface charge concentration and the channel thickness will determine the concentration where the surface-charge-governed behavior gives way to the bulk behavior.

The range of nanochannel widths that permit unipolar transport in water is thus bounded on the large end by the Debye length of deionized water, and bounded on the small end by the molecular limit. If no electrolyte is added, a background ion concentration of 10^{-7} M is still present due to the autoionization of pH 7 water; therefore, the longest Debye length possible in room temperature water is ~900 nm. However, since water is acidified by exposure to air, and additional electrolytes may be added, a more practical upper limit on nanochannel width is ~100 nm. Smaller sizes than that are yet preferable, since a smaller channel permits unipolar transport over a wider range of electrolyte. Meanwhile, the lower limit is defined by the size of the ion being transported

– possibly as small as 0.5 nm. In the vast majority of previous unipolar ionic transport studies, the channel width is in the tens of nanometers – limited perhaps by fabrication capability.

A number of prior works have exploited nanofluidic ion transport to demonstrate appealing proof-of-concept devices.[84] However, the channels used in these devices are mostly fabricated by top-down patterning,[85-86] making them too expensive, too difficult to scale up, and too space-inefficient for many small-scale research labs or for applications such as energy conversion or water desalination. Some progress has been made towards bottom-up assembly of nanofluidic channels.[87-92] All of these methods are still too expensive and slow for application, though they represent a marked improvement over top-down methods. The goal of this work, therefore, is to demonstrate a materials platform that addresses the scaling problem, by using bottom-up assembly to create nanofluidic channels in bulk quantity. Here we will find that reconstructed layered materials are an eminently scalable, inexpensive system that replicate the essential properties of nanofluidic channels.

Graphene oxide paper consists of stacks of solid graphene oxide nanosheets, with the nanosheets oriented parallel to the plane of the paper. The sheets themselves are relatively hydrophilic, and the paper is hygroscopic. As a result, when graphene oxide paper is exposed to moisture, water intercalates between the sheets, hydrating them and swelling the structure. This swelling can be observed via the distinct change of d-spacing between the dry and hydrated states of GO paper (Figure 3.1). The spacing difference between dry and hydrated papers suggests that the water accounts for about 40% of the volume of the hydrated paper, and that hydration contributes an additional 0.6 nm to the width of a layer. By one interpretation, this is the actual thickness of the water layer. However, recall that the structure of a graphene oxide sheet consists

of a graphitic layer (0.35 nm in thickness) from which protrude epoxides, phenols and carboxylate groups. The hydrophilic groups can be expected to mingle favorably with water molecules and dissolved ions. A more accurate picture of the water layer, then, may be a 2-dimensional gallery 1.1 nm in width, into which oxygen atoms frequently intrude from the channel walls. At this time we cannot experimentally discern which depiction of the nanochannel width is more correct. However, we can conclude that the channel width is in the range 0.6 to 1.1 nm, making it one of the narrowest nanofluidic channels ever reported, just large enough to permit transport of small ions. Since the GO sheets lie in-plane, the inter-sheet channels do too.

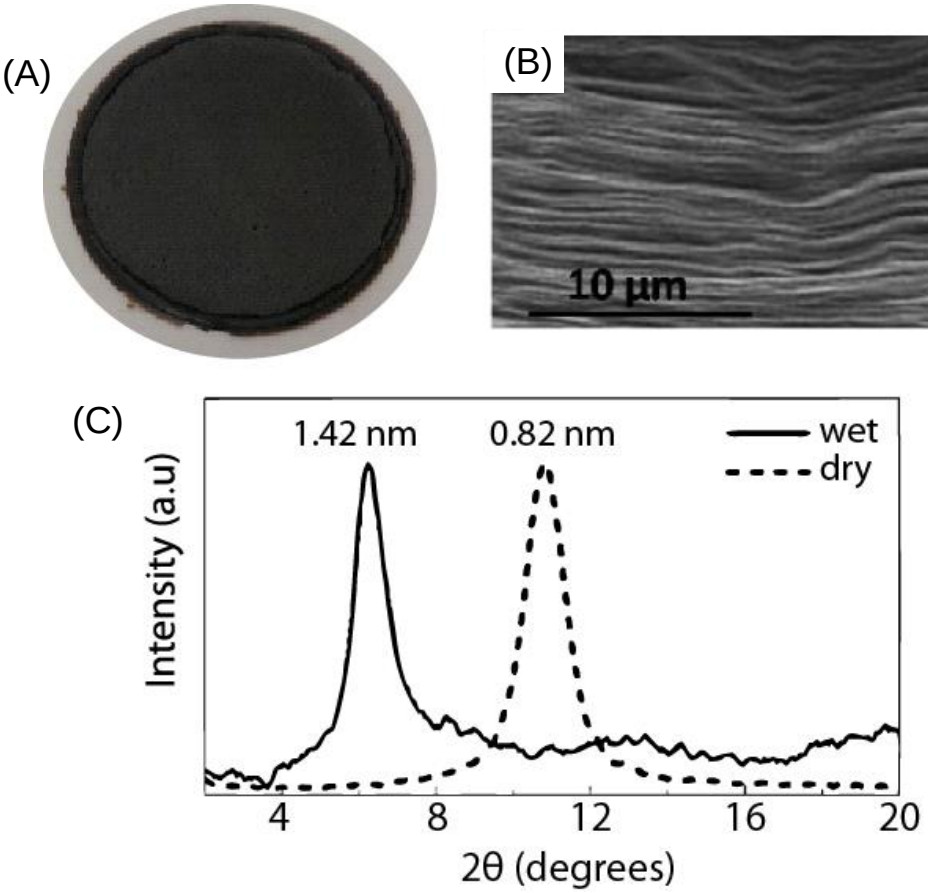

Figure 3.1. Structure of GO nanofluidic paper. *(a) Photograph of macroscopic vacuum-filtered graphene oxide paper. (b) cross-sectional SEM of graphene oxide paper showing layered microstructure. (c) XRD of graphene oxide papers. When GO paper equilibrates with dry air over calcium chloride, a small spacing is observed; when GO paper is moistened, a wider spacing is observed. The 0.6 nm difference is attributed to interlayer water molecules.*

To create a nanofluidic device one needs only to cut the GO paper into the desired shape. Here GO is typically cut with scissors into a rectangular shape ~20 mm × 5 mm. The GO paper thickness is typically ~20 µm, meaning that the device contains 10,000-20,000 parallel layers of nanochannel. The cut device is left to rest in moderate-humidity room air, before sealing in a degassed polydimethylsiloxane (PDMS) prepolymer, and curing the PDMS to form a water-resistant enclosure. The PDMS is cut at the narrow ends of the GO, to create electrolyte reservoirs and to expose the ends of the GO paper to the electrolyte solution. Current – voltage curves were measured through Ag/AgCl wires dipped into the reservoirs. An image of the device setup can be seen in Figure 3.2.

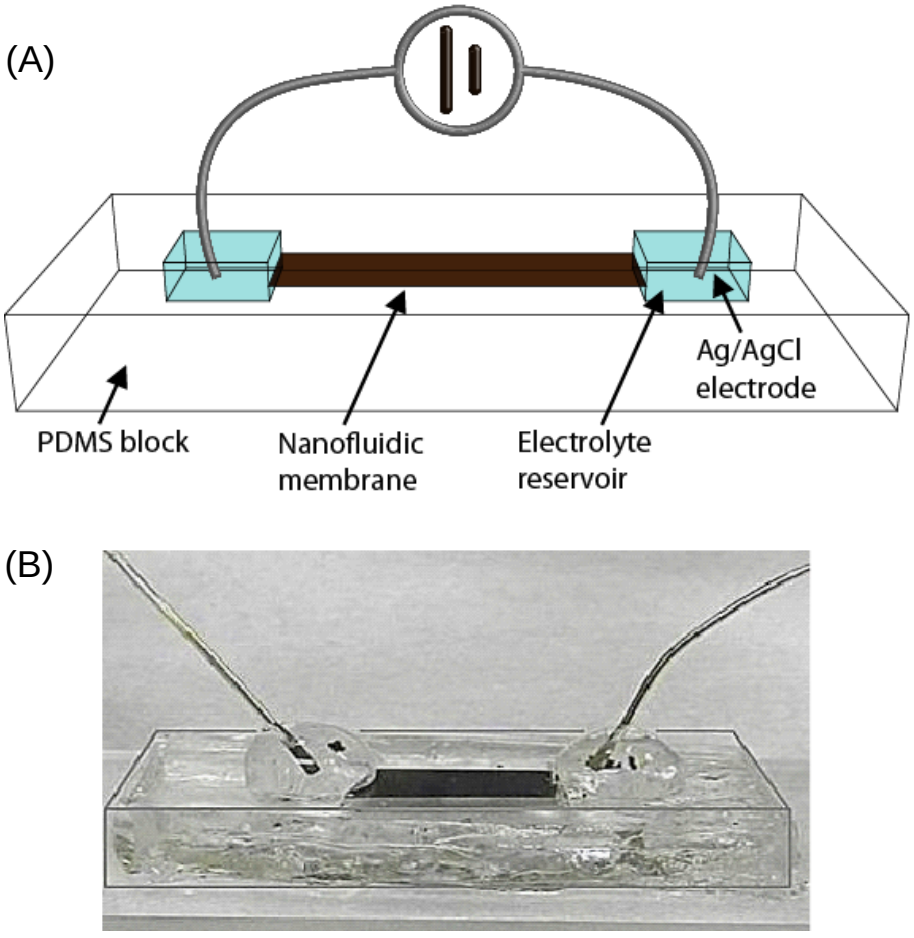

Figure 3.2. *(a) Schematic illustration and (b) photograph of GO nanofluidic test geometry. Thin black lines are superimposed on the photograph (b) to accentuate the outer edges of the PDMS.*

Initially, no current is observed, as the channels are not fully hydrated. Over time, water infiltrates the GO paper and opens up nanofluidic channels, leading to increased ionic current. A 1 cm long device reaches equilibrium hydration in about 45 minutes to an hour. To ensure devices hereafter are tested at equilibrium conditions, GO devices are soaked in deionized water before testing for 2 hours (small devices, <2 cm long) or overnight (large devices, >2 cm). Then, before each measurement, the device is soaked overnight in a bath of the desired electrolyte concentration, so that the larger, slower salt ions can equilibrate as well. Testing is carried out in a two-electrode configuration and conductivity is extracted from the slope of the current-voltage curve.

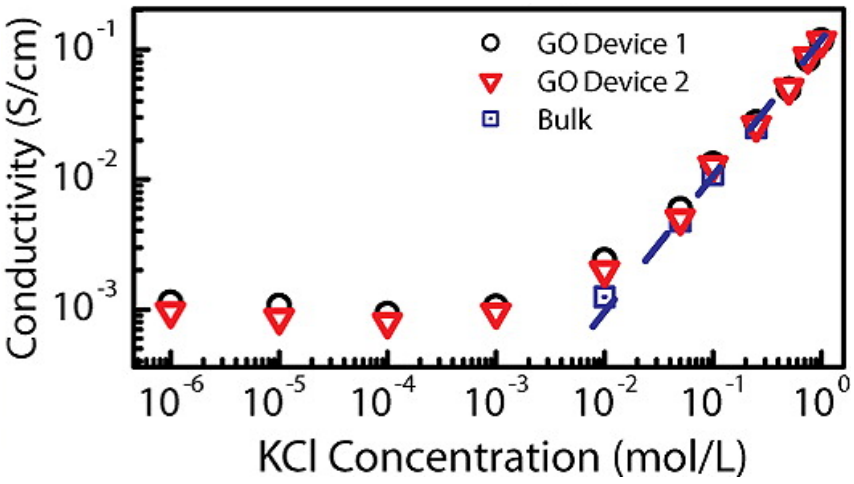

Figure 3.3. Conductivity vs concentration for the GO device shown in Figure 3.2. *At low concentrations, surface-charge governed conductivity dominates, and conductivity through the channels loses its dependence on electrolyte concentration.*

One hallmark of a nanofluidic channel is the existence of the surface-charge-governed regime, where conductivity is independent of concentration because the bulk ionic conductivity is negligible in comparison to the surface conductivity. This behavior is clearly visible in the conductivity-current curve shown in Figure 3.3. At high salt concentration, ionic transport through the GO nanochannels scales linearly with concentration, as it would in a bulk electrolyte solution.

However, the nanochannels begin to deviate from the bulk ionic conduction behavior at concentrations of about 10^{-2} M. Below that point, the conductivity plateaus and becomes constant with respect to concentration, characteristic of surface-charge-governed transport. In this regime, the negative charge fixed to the GO sheets attracts cations into the channels while repelling anions, causing the cation concentration in the nanochannels to considerably exceed that in the electrolyte bath. The enriched concentration in turn leads to ionic conductivity values far greater than would be observed in bulk. For the sake of direct comparison, a bulk scale channel is carved out of PDMS and current-voltage curves are recorded for the same electrolyte concentrations. Indeed, the bulk conductivity is similar to the nanochannel conductivity at high salt concentrations, but the values diverge as the electrolyte concentration drops into the nanochannels' surface-charge governed regime (Figure 3.3). This property is observed for other electrolytes too.

The surface charge density can be estimated by graphical means using the concentration-conductivity data from Figure 3.3. If equations 3-5 indeed hold true for the intermediate concentrations in between the two regimes, then it follows that there exists a point where:

$$\sigma_{bulk} = \sigma_{SCG}$$

$$\sigma_{total} = 2\sigma_{bulk} = 2\sigma_{SCG}$$

Straight line fits from the low-concentration and high concentration limits of the curve can be translated upwards by a factor of 2, and then extrapolated until they intersect. The point of intersection should lie on the experimental curve, at a concentration where:

$$\sigma_S = \frac{C_B\, N_A h\, q}{2\, t}$$

where $t \equiv \frac{\mu_+}{\mu_+ + \mu_-}$ is the transference number of the electrolyte. Carrying out this approximation method, we can estimate the GO surface charge density to be 0.8 mC/m^2 within the range of values typically reported in literature.

Note that the current values throughout Figure 3.3 are in the microampere range, far higher than nanofluidic devices assembled by other means. This difference reflects the unprecedently massive scale of the devices shown here. Where top-down devices typically consist of only a single channel, nanoscopic in scale, the GO paper device contains thousands of parallel nanochannels in a microns-thick stack. If larger cross-sectional areas are desired, multiple slices of GO paper can easily be stacked in parallel. The stacks can even be "welded" together by using small amount of water to locally dissolve GO sheets at the surface. Since GO sheets are much smaller than the final GO paper, it follows that the layers of 2D nanochannels are interconnected to form a percolated network within the GO paper. At sheet edges and voids, ions can cross between one nanochannel layer and the next. Ion transport is allowed in the vertical direction (which is to say, the direction that is normal to the GO paper); however, since sheet edges and voids are few and far between, ions will have to follow a tortuous, switch-backed path in order to move vertically across the GO paper. Consequently, we should expect ionic conductivity to be considerably lower in the vertical direction, with the magnitude of this difference determined by the prevalence of sheet edges and voids. Indeed, an orders-of-magnitude difference is observed between vertical (cross-plane) ionic conductivity and horizontal (in-plane) ionic conductivity.

Taken together, these core features and observations show 2D nanofluidic paper to be a compelling platform for further nanofluidic studies. The facile, low cost assembly techniques

allows researchers to explore ideas that are too naïve or too risky to warrant the time and capital expenditure that conventional nanofluidics work would entail. Perhaps the single most important benefit of 2D nanofluidic paper is that it lowers the barrier to entry for researchers interested in carrying out their own nanofluidics experiments. The following chapters will explore two studies carried out on 2D nanofluidic paper, which might have been infeasible to pursue were I required to use conventional nanofluidics fabrication methods.

CHAPTER 4

TWO-DIMENSIONAL NANOFLUIDIC PROTON TRANSPORT THROUGH A RECONSTRUCTED INORGANIC NANOLAMELLAR MEMBRANE

Graphene oxide paper has been shown to fulfill the essential requirements of a nanofluidic channel array. However, there is no reason to suppose that 2D nanofluidic performance is uniquely linked to the specific chemical moieties present in graphene oxide. Instead, the properties are expected to derive from the tightly-packed lamellar microstructure, the uniform geometry of the 2D channel, and the presence of fixed charges on the channel walls. High aspect ratio 2D sheets, regardless of material composition, have a unique advantage over other morphologies in that they are the only shape that can stack to yield interstitial spacing that is both percolated throughout the material and highly uniform in size and orientation. The width of such lamellar channels is similar

to the size of solvated ions as well as the Debye length of electrolytes at up to physiological concentrations. The charges and the confined geometry exclude co-ions and give rise to unipolar transport.[93] Meanwhile, the microstructure yields a percolated network of hydration channels throughout the film, allowing macroscopic GO paper pieces to function like a "bulk" nanofluidic channel material.[94-98] If a different 2D material could be exfoliated into a dispersion of charged hydrophilic sheets, then reassembled into a paper-like film with lamellar microstructure, that film might similarly be expected to show characteristics of nanofluidic ion transport. Indeed, we will find that aluminosilicate minerals can be processed to create a clay mineral nanofluidic membrane, which is a functioning inorganic analogue to the GO nanofluidic membrane discussed previously.

Clay minerals are naturally occurring hydrous aluminosilicate minerals that exist in the form of micron-sized flat platelets.[99-100] They form in the presence of water, by weathering or hydrothermal alteration of other aluminosilicates, and are often a major component of soils and sedimentary rocks. Compared to graphene oxide, clay minerals offer several properties that may be advantageous: (1) the starting material is cheaper and more abundant; (2) they can be exfoliated by ion exchange,[101-102] under conditions that are much milder and more environmentally benign than the chemical exfoliation of graphite; (3) they are stable to a wider range of temperatures and reagents than their organic counterparts; (4) they are a more diverse family of materials, offering a range of charge sign and charge density choices. In this work we construct nanofluidic channels from vermiculite, a common clay mineral that finds widespread use in construction and soil applications.

Vermiculite is a 2:1 clay, with each layer consisting of one octahedral sheet sandwiched between two tetrahedral sheets, as illustrated in Figure 4.1a.[100] The sheet contains a net negative

charge, balanced by interlayer cations. Some variation in cation and water content is possible, but a typical structural formula for vermiculite is $(Mg,Fe^{+2},Fe^{+3})_3(Al,Si)_4O_{10}(OH)_2 \cdot 4H_2O$. Vermiculite crystals can be partially exfoliated by thermal shock, which rapidly vaporizes water inside the material and pushes the sheets apart into a low-density accordion structure. Further exfoliation can be accomplished by replacing the multivalent cations with monovalent potassium ions, to weaken the attractive forces holding the crystal together. The layers are pried apart further by subsequent exchange of the potassium ion to lithium, which has a larger hydration diameter.[102] Finally, the ion-exchanged vermiculite is treated with hydrogen peroxide, so that in-situ oxygen evolution can agitate the sheets and push them still farther apart.[103] A considerable amount of solid clay particles remain unexfoliated after this process, however we do obtain a stable exfoliated dispersion as well.

This method yields a vermiculite dispersion that physically resembles graphene oxide in certain ways. The colloidal suspension of exfoliated vermiculite, shown in Figure 4.1c-d, is a milky golden brown, with bands and optical schlieren readily appearing when it is swirled. Vermiculite dispersions display strong birefringence when viewed through crossed polarizers, indicating nematic liquid crystalline ordering as would be expected from a dispersion of high-aspect-ratio particles.[59] In Figure 4.1e-f, the exfoliated vermiculite particles are examined by microscopy. SEM of the particle population finds they mostly range around 1-10 microns in lateral size. AFM is used to assess the thickness of exfoliated flakes, and the thinnest flake observed is ~3 nm in thickness, consistent with a bilayer. No monolayer flakes were directly observed, and the sample is thought to consist mostly of few-layer flakes. Like graphene oxide, vermiculite dispersion can be readily reassembled by vacuum filtration or casting to form a freestanding paper-like thin film.

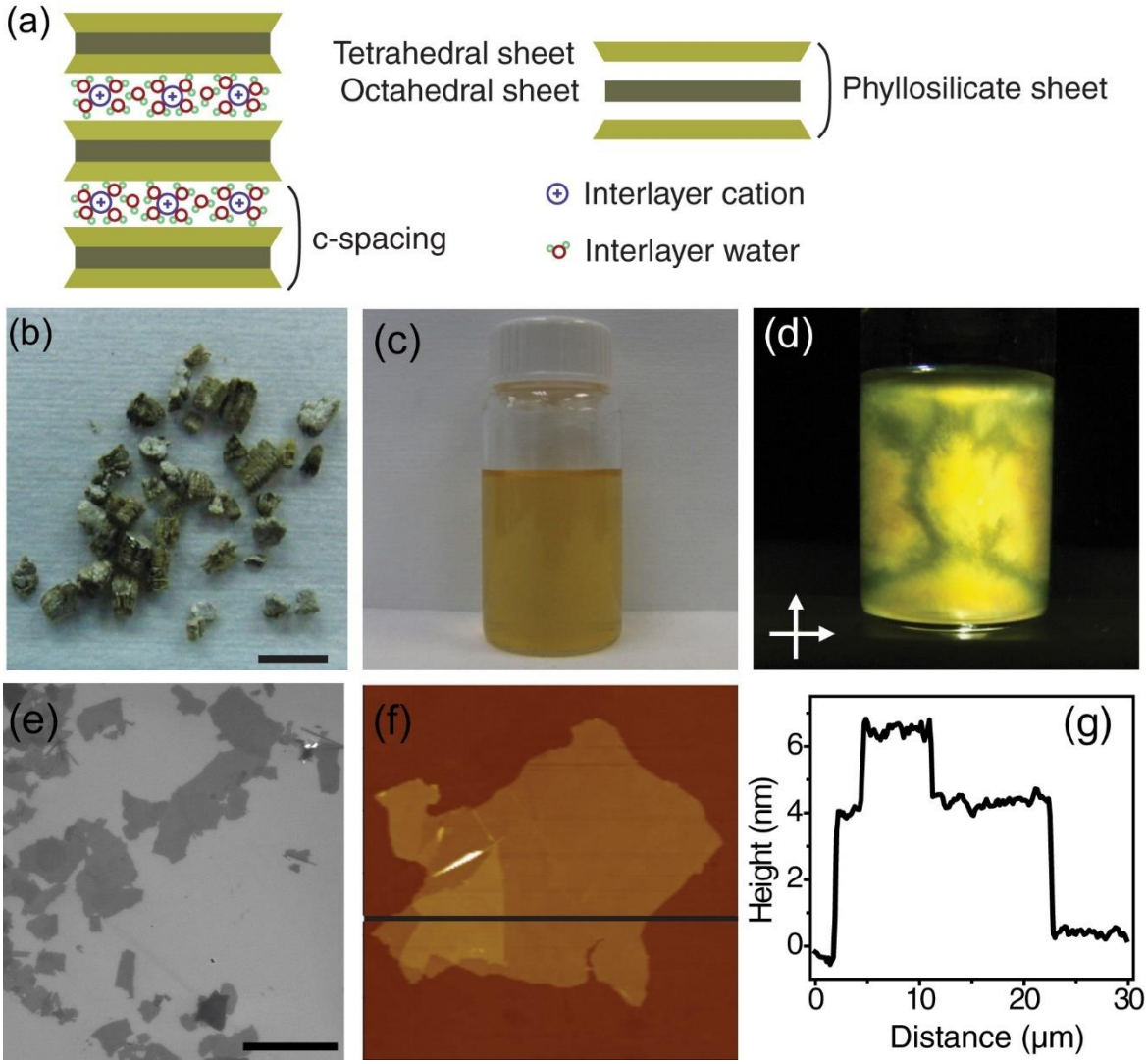

Figure 4.1. Exfoliation of vermiculite crystals and resulting dispersions of few-layer flakes. *(a) Structural model of vermiculite layers. (b) Thermally expanded vermiculite crystals (scale bar 5 mm), which can be exfoliated by ion exchange to form (c) a single to few layer dispersion in water. (d) The dispersion exhibits strong birefringence when viewed through crossed polarizers, suggesting nematic ordering originating from the high aspect ratios of the flakes. (e) SEM (scale bar 50 μm), (f) AFM image, and (g) corresponding AFM height profile of exfoliated flakes shows that they are few-layer stacks with lateral dimensions of tens of microns.*

The paper-like exfoliated reconstructed vermiculite membrane (hereafter abbreviated "VMT paper") resembles GO paper in many of its key physical properties. Cross-sectional SEM (Figure 4.2b) shows that, like GO paper, VMT paper has a lamellar microstructure with stacks of

nanosheets oriented parallel to the plane of the macroscopic paper. VMT paper can be assembled at a variety of controlled thicknesses, depending on the amount of exfoliated vermiculite solids used; typically, VMT papers used here are 10 – 30 μm thick. While VMT paper seems qualitatively more brittle than GO paper, it can still be cut, bent, twisted and folded with little difficulty.

Like GO paper, VMT paper shows a lamellar atomic ordering with hydration-dependent interlayer spacing, indicating that the solid layers are pushed apart to accommodate the formation of hydration channels. X-ray diffraction (XRD) of the starting vermiculite particles and of VMT papers reveals changes in the spacing. Multiple interlayer spacing values are possible in natural vermiculite (even within the same sample), due to the variety of possible interlayer cations, different degrees of hydration, and interlayer structures. Indeed, as shown in Figure 4.2c, the thermally expanded vermiculite particles used as our starting material display four coexisting [001] peaks. The peaks centered at $2\theta = 7.3°$ (d = 12.1 Å) and 6.1° (d = 14.5 Å) correspond to the {001} d-spacings of Mg-vermiculite with one and two hydration layers, respectively. The peak at $2\theta = 8.6°$ (d = 10.3 Å) is attributed to the {001} diffraction of K-vermiculite, and the small peak at 7.1° (d= 12.4 Å) is attributed to an interstratified phase with intermediate layer spacing. However, after vermiculite layers were exfoliated and reconstructed into VMT paper, they showed a single homogenous layer spacing of $2\theta = 6.2°$ (d = 14.1 Å) as shown in Figure 4.2d, in agreement with a lithium-intercalated vermiculite with two water monolayers intercalated into each channel. Does the exfoliation process replace all the various interlayer cations and hydration states in the original vermiculite with a single interlayer cation and a single hydration state, thereby homogenizing the sample? Or, does the process selectively exfoliate a specific subset of vermiculite channels? The unexfoliated residual material does not appear noticeably different from starting material in XRD,

suggesting that the first of these two explanations is the correct one. But, the latter cannot be ruled out. Either way, the exfoliation-reassembly process effectively "refines" the vermiculite to create a more uniform lamellar structure with well-defined interlayer spacing.

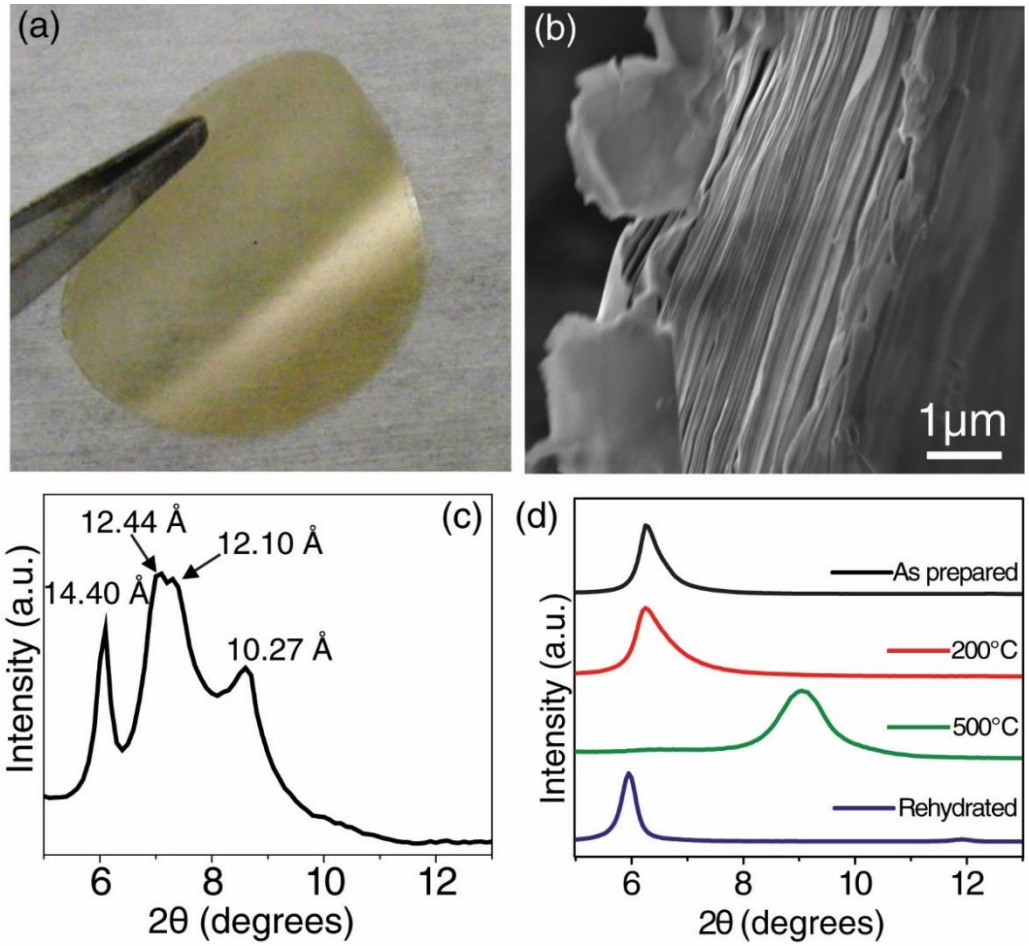

Figure 4.2. XRD characterization of VMT paper lamellae. *(a) A photo showing a flexible free-standing vermiculite membrane obtained by filtration. The lamellar structure is clearly shown in (b) the cross-sectional SEM image. (c) XRD patterns of unexfoliated vermiculite particles and (d) the re-constructed vermiculite membranes before and after thermal and rehydration treatments.*

The interlayer spacing of VMT paper, measurable by XRD, can be correlated with its degree of hydration. Over the course of exfoliation and filtration, vermiculite sheets become amply hydrated, showing a prominent {001} peak that corresponds to a vermiculite with two intercalated water monolayers per structural unit. To support the claim that the interlayers are indeed propped

open by water rather than another component, XRD patterns are recorded on VMT paper dehydrated in a dry oven. As the VMT becomes drier, then interlayer spacing drops in discrete steps. With mild heating, bilayer water and monolayer water peaks coexist. With further heating, the VMT paper can be converted to smaller, dehydrated states. Exposure to moisture gradually restores the dehydrated VMT paper to its fully hydrated interlayer spacing.

VMT paper nanofluidic devices can be prepared in much the same way as GO devices. The VMT paper is cut with a razor blade into the desired shape, typically a rectangle ~20 mm × 7 mm. The sample is then immersed in degassed PDMS prepolymer, which is cured to form a water-resistant enclosure for the device. The PDMS is cut, exposing the ends of the VMT paper rectangle to an aqueous electrolyte or acid solution for testing. Before each test, the device ends are exposed to the desired electrolyte solution overnight, so that the device has time to fully equilibrate. Current – voltage curves are measured through Ag/AgCl wires dipped into the reservoirs. Testing is carried out in a two-electrode configuration and conductivity is extracted from the slope of the current-voltage curve. An image of the device setup can be seen in Figure 4.3.

Like GO paper, VMT paper displays surface-charge-governed cation transport, a characteristic property of a nanofluidic channel. This can be seen in the data presented in Figure 4.3d. At high cation concentration, the relationship between concentration and conductivity is a simple linear scaling, meaning that the membrane conducts like a bulk electrolyte solution. The VMT nanochannels begin to deviate from the bulk behavior at about 10^{-2} M. For concentrations lower than that, the conductivity plateaus towards a constant value with respect to concentration. This plateau is the signature of surface-charge-governed conductivity, and its onset reflects the point where the Debye length of the solution becomes greater than the distance between the fixed

charges on opposite channel walls. Since the channel walls are negatively charged, the surface-charge-governed regime permits transport of only the cations, and the cation concentration in the channels is determined by the surface charge density rather than by the concentration of the electrolyte. At the onset of this behavior, the proton conductivity is 2.6×10^{-2} S cm^{-1}, decreasing to 6.0×10^{-3} S cm^{-1} at the lowest concentration tested – in other words, conductivity decreases by a factor of 5 as concentration changes by a factor of 10^5. By contrast, the bulk electrolyte channel conductivity decreases in direct proportion to concentration over the entire range of concentrations tested. Surface-charge-governed behavior explains the observation of concentration-insensitive greater-than-bulk proton conductivity in charged vermiculite nanochannels.

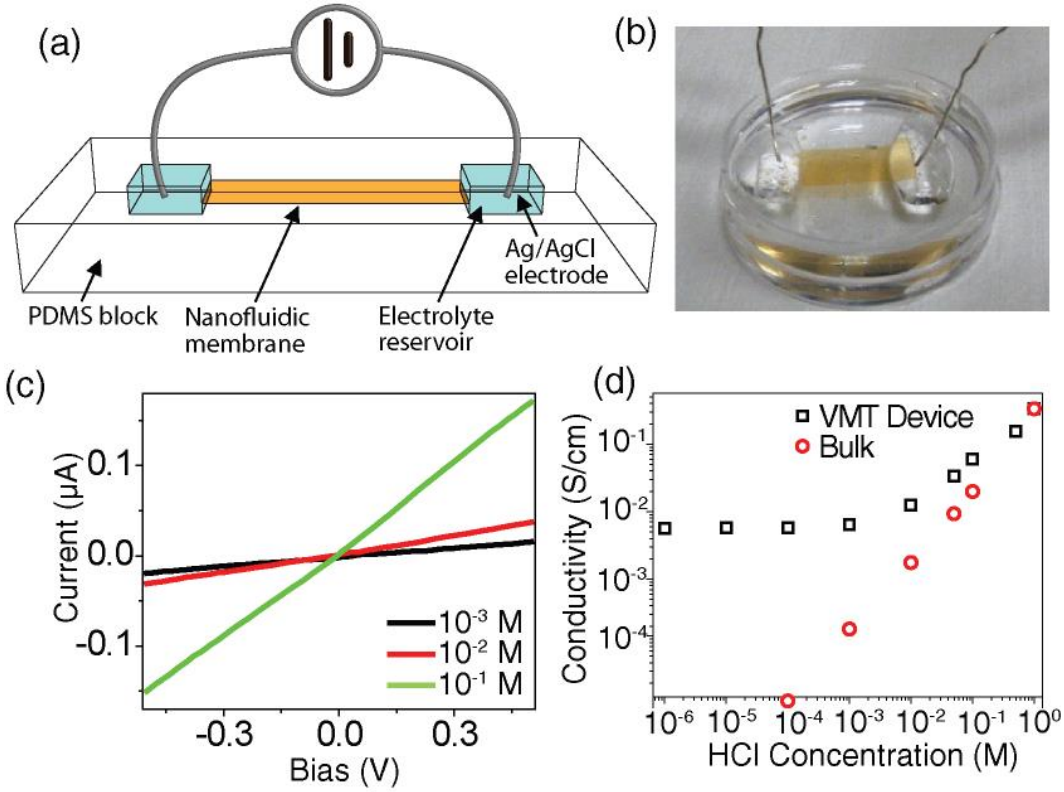

Figure 4.3. VMT paper nanofluidic device. *(a) Schematic illustration and (b) photograph of a VMT paper nanofluidic device. (c) Representative IV curves of a VMT paper device. (d) Plotting the channel conductivity as a function of concentration, we observe the hallmark of nanofluidic devices, a transition between bulk-like (>10^{-2} M) and surface-charge-governed (<10^{-3} M) ionic conductivity regimes. The conductivity of bulk hydrochloric acid is measured as a reference.*

The effects of temperature and isotopic substitution are examined in order to uncover mechanistic information about the proton conduction of this system. To study the effect of temperature, a VMT paper membrane and a thermometer were embedded together into a thick (~3 cm) PDMS block, so that current – voltage measurements could be carried out in a heated silicone oil bath. This experimental setup is illustrated in Figure 4.4a. Conductivity was then measured as a function of temperature for an electrolyte concentration of 10^{-4} M, well within the bounds of the surface-charge-governed regime. The relationship between conductivity and temperature can be described by a variation of the Arrhenius equation:

$$S = A \exp(-\frac{E_a}{k_b T})$$

where S is the conductivity, E_a is the activation energy, T is absolute temperature, and A and k_b are constants. As shown in Figure 4.4b, the data indeed match an Arrhenius fit with activation energy of 0.19 eV. The low activation energy suggests that protons are transported by a Grotthuss mechanism.[104-105] In this mechanism, charge is transported by the coordinated hopping of protons between water molecules in the nanochannels. This mechanism is consistent with the structural model of vermiculite, in which a continuous network of water molecules fills the galleries between layers.

An independent verification of protonic conductivity was carried out by isotopic substitution. Hydrogen ions and atoms in the hydrated vermiculite were exchanged with deuterium ions and atoms by soaking the membranes repeatedly in baths of the corresponding DCl / D_2O solutions. Conductivity was then measured using DCl / D_2O as the electrolyte, and was found to decrease by a factor of 1.6 ± 0.1 compared to the conductivity of the same device in HCl / H_2O.

This conductivity shift is reversible – conductivity can be restored by soaking in HCl / H_2O, and returned to its deuterated value by soaking again in DCl / D_2O. We conclude that the difference in the mass of the charge carrier is responsible for this conductivity difference. If charge is carried by the hopping of individual protons, as it is in the Grotthuss mechanism, then the isotope effect ratio will be approximately $\sqrt{(Z_D/Z_H)}$, or ~1.5. If, on the other hand, protons are carried by a vehicular mechanism such as the diffusion of H_3O^+ ions, or the charge carrier is a different ionized species in the system, then the isotope effect ratio will merely be commensurate with the viscosity ratio between D_2O and H_2O, ~1.2.[106-107]

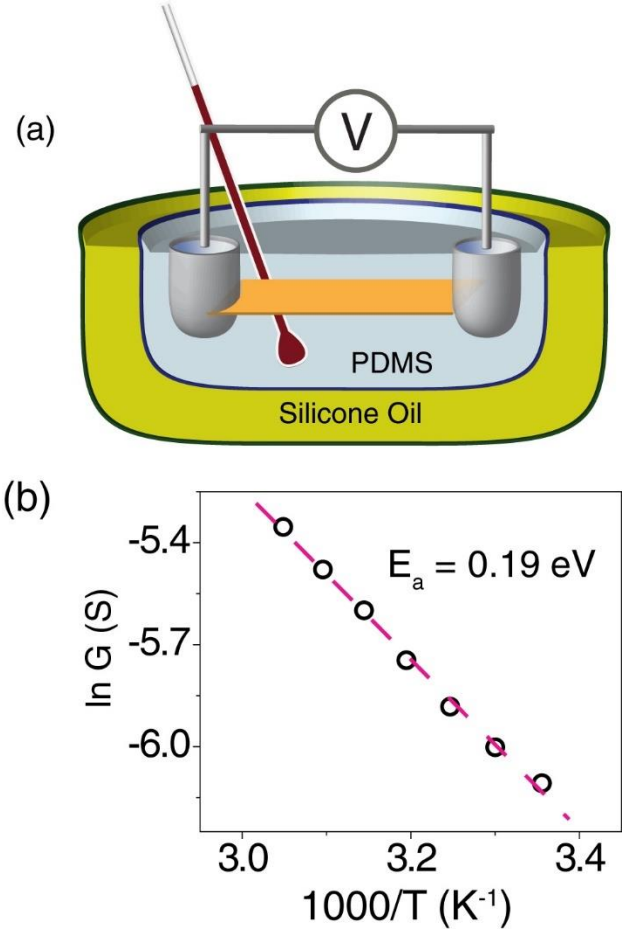

Figure 4.4. Temperature-dependent conductivity reveals a Grotthuss-like activation energy. *(a) Schematic illustration of device setup, used to ensure even heating and monitor internal temperature. (b) A plot of conductivity against temperature reveals Arrhenius-like behavior with an activation energy of 0.19 eV, consistent with Grotthuss transport of charge carriers.*

The surface charge density of the channel walls is a value we should like to know, as it plays an important role in determining the performance of the nanofluidic VMT paper. Additionally, so long as we operate in the surface-charge governed regime, the surface charge density dictates the concentration of charge carriers inside the nanochannels. That means the surface charge density (σ_S) can be used to relate the ionic conductivity (Λ_S) to the mobility (μ), according to the relationship:

$$\Lambda_S = \mu \sigma_S e$$

Two methods can be used to estimate the surface charge density. In the first method, the membrane is redissolved in water, and a galvanometric titration is used to determine the ion exchange capacity of the clay. This approach is adapted from a method used to determine the charge densities of Nafion and other proton-conducting polymers.[108] In the second method, surface charge density is estimated by identifying the concentration where surface-charge-governed transport and bulk transport contribute in equal measure to the membrane conductivity. The latter approach is adapted from previous studies on nanofluidic channels,[109] and was used in a previous chapter to estimate the surface charge density of GO paper. Fortunately, both methods agree!

The ion exchange capacity is a value of particular interest to ion exchange membranes, and can be used to estimate the surface charge density if the nanogeometry of the system is well known. Here we estimate the ion exchange capacity of vermiculite by titration, and divide that value by the channels' surface area. A vermiculite membrane (c.a. 100 mg dry weight) is first oven dried until Fourier transform infrared spectroscopy indicates complete removal of water. Then it is immersed in 2 mL of 1 mM HCl overnight, after which it is observed to dissolve into loose

sediment.[110] The H^+ in the solution exchanges with the Li^+ ions in the interlayer spaces, and the conductivity of the electrolyte drops due to the conductivity difference between HCl (limiting conductance 425 Ω^{-1}) and LiCl (limiting conductance 115 Ω^{-1}).[111] The change in solution conductivity of the supernatant is used to infer the amount of H^+ that had exchanged to Li^+. The presence of lithium in the supernatant is confirmed by drying an aliquot and carrying out X-ray photoelectron spectroscopy (XPS) on the residue. The total surface area of the film can be calculated from its mass, knowing the density and interlayer spacing of the material. From all of this, the surface charge density is calculated to be 1.4 mC m^{-2}. From this value and the channel conductivity at low concentration, we find the proton mobility to be 1.2×10^{-3} $cm^2\ V^{-1}\ s^{-1}$. A representative sample measurement is shown in Figure 4.5. For comparison, the mobility of vermiculite is comparable to the commercial proton conductor Nafion.[108, 112]

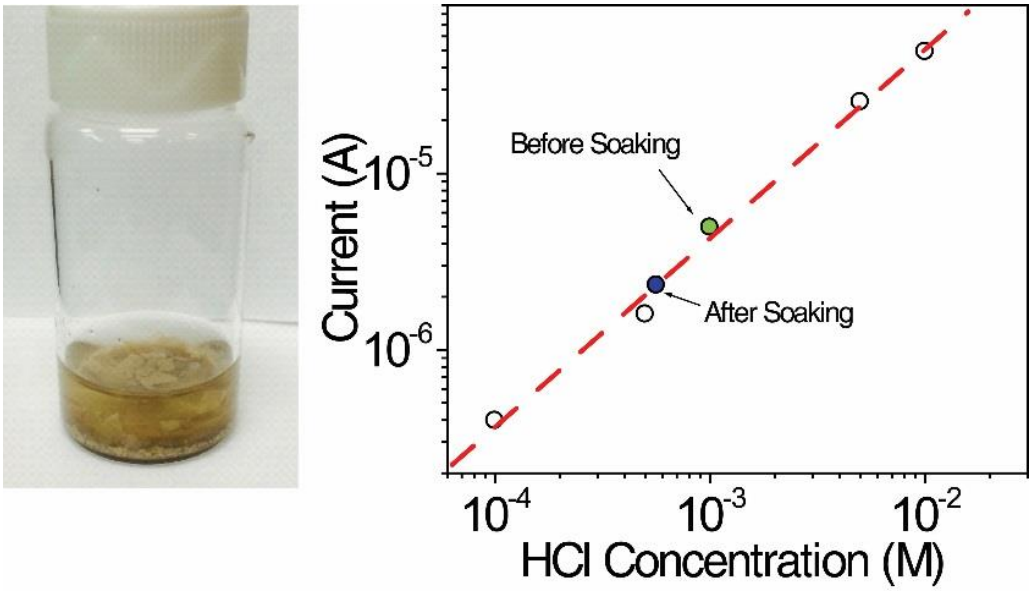

Figure 4.5. Ion exchange capacity via galvanometric titration. *(a) A typical sample of oven dried, dehydrated vermiculite membrane, soaked in 2 mL of 1 mM HCl overnight to exchange the Li^+ with H^+. (b) Conductivity measurements taken on the supernatant of this sample are imposed on a calibration curve showing the conductance of HCl solution at the concentration range of 10^{-4} to 10^{-2} M. The filled circles in green and blue colors marked the conductance of the HCl supernatant before and after exchanging with the dried vermiculite membrane. In this sample, 9×10^{-7} mol of protons were immobilized by 109.1 mg of dry vermiculite membrane.*

An independent estimate of surface charge density (and thus mobility) can be taken directly from the graph of concentration versus conductivity.[109] The ionic conductance through the nanofluidic channels (G) is approximately equal to the sum of a bulk-like conductance (G_B) which dominates at high concentration, and a surface-charge-governed conductance (G_S) which dominates at low concentration. It follows that there exists a reservoir concentration C_B, where $G_B = G_S$, and therefore $G = G_B + G_S = 2G_B$. Bulk conductance is linearly-dependent on the concentration and is described by:

$$G_B = q(\mu_H + \mu_{Cl})C_B N_A w(h/l)$$

where μ_H and μ_{Cl} are the mobilities of H^+ and Cl^-, N_A is Avogadro's number, q is elementary charge and l, h, and w are the length, height, and width of the channel, respectively. Surface charge governed conductance is described by:

$$G_S = 2\,\mu_H \sigma_S (w/l)$$

When $G_B = G_S$, we can combine the two equations to deduce:

$$\sigma_S = \frac{C_B N_A h\, q}{2\, t_{H_{bulk}}}$$

where the proton transference number is

$$t_{H_{bulk}} \equiv \frac{\mu_{H_{bulk}}}{\mu_{H_{bulk}} + \mu_{Cl_{bulk}}}$$

$t_H = 0.5$ represents a system where cations and anions contribute equally to the ionic conductivity, and $t_H = 1$ represents a system where current is carried entirely by the cations (as is

the case for our system at the surface-charge-governed limit). $t_{H_{bulk}}$ has been measured at around 0.85 in bulk HCl.[113-114] We assume here that the bulk term of the conductance has a transference number of 0.85, and the surface-charge governed conductance is completely cationic. The actual transference number of the system could be concentration dependent, varying from a bulk-governed limit of 0.85 to the surface-charge-governed limit of unity. It's also possible that the confines of the nanochannel walls hinder the larger anions more than the smaller cations, giving a greater-than-bulk transference number even in the bulk part of the equation. If that's true, then our operating assumptions will slightly underestimate the proton mobility.

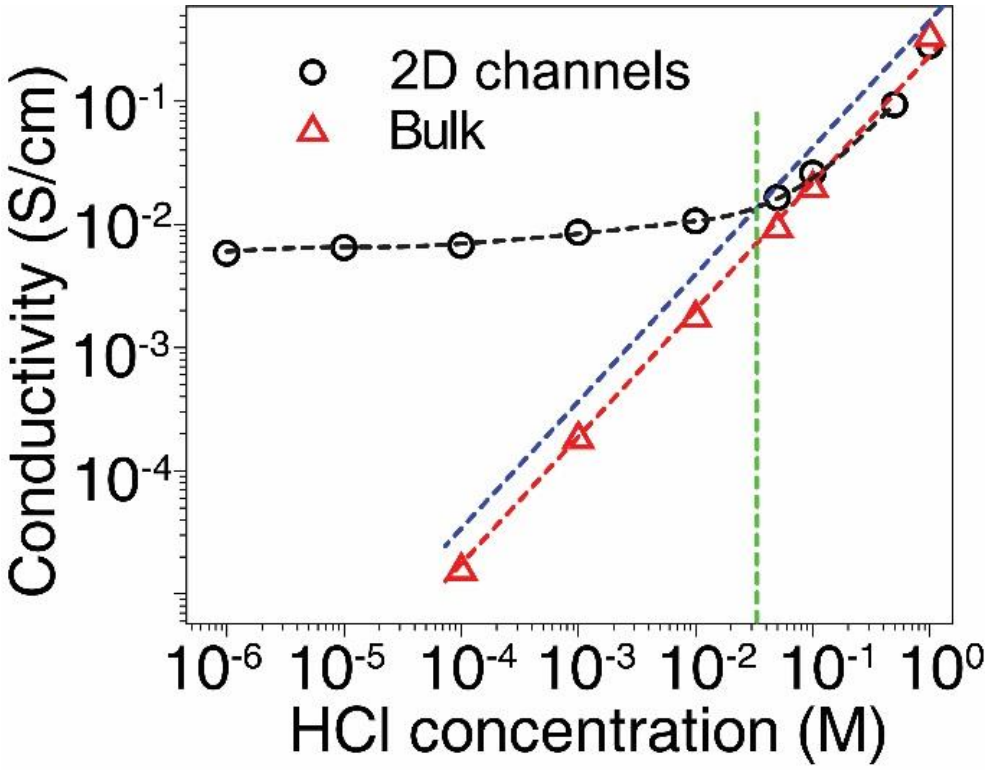

Figure 4.6. Calculating surface charge density using the conductivity curve. *Guidelines are overlaid on top of the data from Figure 4.3d. Black and red dashed lines represent the channel and bulk conductivities, respectively. The blue line is double the bulk conductivity. The blue and black lines intersect at the point where $G = 2G_B$, and at this point the surface charge contribution is equal to the bulk contribution.*

Figure 4.6 illustrates the graphical method with guidelines overlaid on top of the data from Figure 4.3d. Black and red dashed lines represent the channel and bulk conductivities, respectively. The blue line represents doubled values of bulk conductivity. The intersection between black and blue lines represents the point where $G = G_B + G_S = 2G_B$. C_B is the concentration where the blue and black curves intersect (green line), approximately 35 mM. Applying the above relationship, we find $\sigma_S \approx 1.0$ mC m^{-2} and $\mu_H \approx 1.8 \times 10^{-3}$ cm^2 V^{-1} s^{-1}.

An advantage of using aluminosilicate minerals rather than organic materials to construct proton channels is their improved thermal stability. Graphene oxide is known to undergo spontaneous disproportionation reactions at temperatures below 200°C; and, in a mildly reductive environment, GO can convert to rGO at room temperature.[115] Inorganic sheets can easily survive greater temperatures. The improved stability of VMT paper can be seen in thermogravimetric analysis (Figure 4.7a). Upon heating, hydrated VMT paper initially experiences a rapid weight loss of about 4.8% before 100°C, and another 1.2% between 100°C and 200°C. Next, it experiences a slow weight loss of an additional 5%, and becomes stable against further weight loss after reaching 855°C. XRD studies (Figure 4.2d) revealed that annealing the membrane at 200°C for a day does not affect its interlayer spacing, suggesting that the initial 6% weight loss observed in thermogravimetric analysis might correspond to the removal of physisorbed water. The interlayer spacing decreases from 14.1 to 9.8Å after annealing at 500°C due to removal of interlayer water molecules. However, the membrane can be readily rehydrated, rehydrating the membrane and expanding it to its previous interlayer spacing (Figure 4.2). After annealing at 900°C, the membrane still had a lamellar structure, but became chalky, brittle, and hard to handle. Figure 4.7b compares proton conductivities through a vermiculite membrane at different pH values

before and after thermal annealing in air for 1 day. Once rehydrated, the conductivity of the vermiculite membrane is apparently unaffected by having been annealed at 200°C, or even 500°C, even though such high temperatures would have devastated the performance of a comparable GO paper membrane.

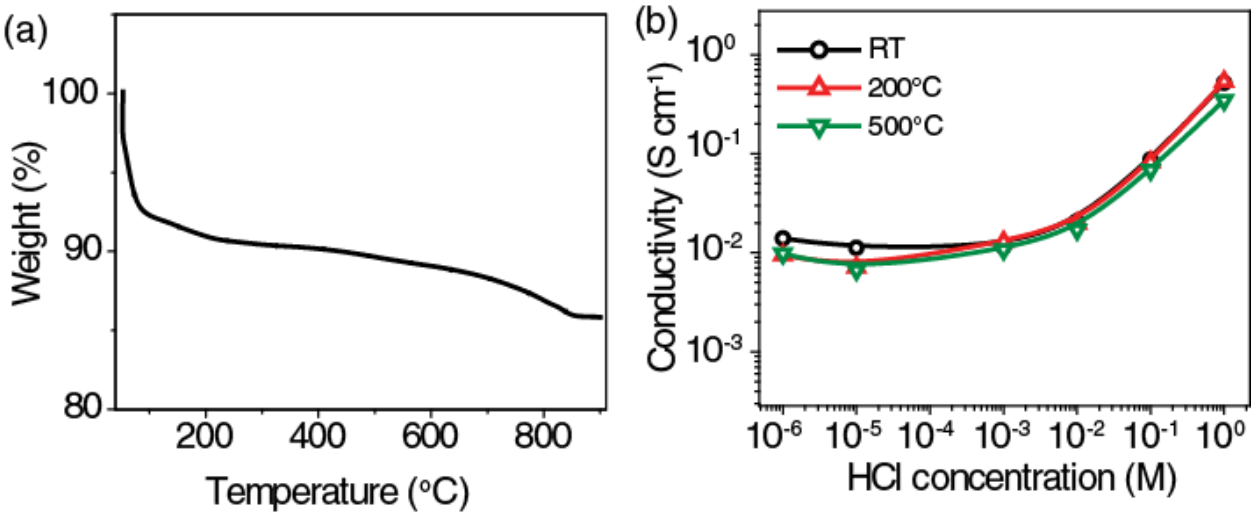

Figure 4.7. Thermal stability of VMT paper devices. *(a) TGA shows the gradual loss of interlayer water as the sample is heated from 100 – 850°C. (b) After annealing at high temperatures, devices can be rehydrated, and their ionic conductivity is almost completely unaffected.*

In summary, we find that thermally stable 2D proton channels can be readily constructed by the restacking of exfoliated vermiculite sheets. While the surface charge density of GO is highly sensitive to the pH of the solution, that of vermiculite is more stable against pH changes, rendering it suitable for proton exchange membrane applications. Surface-charge governed proton conductivity, exceeding that of bulk solution, is observed in VMT paper for all pH values above 2. The conductance of the nanofluidic channels is relatively constant over orders of magnitude variation in proton concentration. The influence of temperature and isotopic substitution indicate that the proton transport mechanism is based on hopping through water molecules in the nanofluidic channel. The surface charge density of the vermiculite walls was determined to be

around 1.4 mC m^{-2}, and the proton mobility in the channel was elevated somewhat higher than bulk, at 1.2×10^{-3} $cm^2 V^{-1} s^{-1}$. VMT paper has extraordinary thermal stability. Even when annealed in air to a state of full dehydration, the material maintained its lamellar structure, and could be readily rehydrated to restore ionic conductivity. Like GO paper before it, VMT paper is a useful model system for construction of nanofluidic devices, with some added benefits. The membrane-like material can be assembled quickly at large scale with cheap materials and simple processing techniques. Perhaps the most important contribution of this work is that it lowers the barrier of entry for researchers who want to study confined ionic behaviors. VMT paper offers a readily accessible platform to accelerate discoveries in potential applications of nanofluidics such as sensing, catalysis, and energy harvesting.[116-118]

Methods

Chemicals. Thermally expanded vermiculite crystals, sodium chloride, potassium chloride, lithium chloride, deuterium oxide, and deuterochloric acid were purchased from Sigma Aldrich and used as-received. Aqueous hydrogen peroxide (H_2O_2) and hydrochloric acid were purchased from Avandor Performance Materials and used as-received.

Preparation of vermiculite membranes. The thermal expanded vermiculite crystals were subjected to a two-step ion-exchange method. 1 g of vermiculite crystals in 500 mL of 5 M aqueous sodium chloride (NaCl) solution were heated under reflux for 24 hours, then collected by vacuum filtration and repeatedly washed with de-ionized (DI) water and ethanol. The as-obtained product was redispersed in 2 M lithium chloride (LiCl) solution and again heated under reflux for an additional 24 hours, followed by vacuum filtration and extensive washing with DI water and

ethanol. The product was then dispersed in water with the help of magnetic stirring and centrifuged at 6000 rpm for 10 min to obtain a jelly-like vermiculite slurry. Finally, the supernatant slurry was filtered through an anodic alumina membrane to obtain light yellow colored flexible vermiculite films, which can be easily peeled off upon drying.

Characterization. The thickness of the exfoliated vermiculite layers was determined by non-contact AFM (Park XE-100). The thickness of the membranes was determined by profilometry (Dektak 150) or cross-sectional SEM. The proton transport measurements were carried out on a probe station equipped with a Keithley 2601A source meter inside a Faraday cage. XRD patterns were recorded using a Rigaku SmartLab diffractometer with Cu Kα radiation.

Preparation of the nanofluidic devices. Apart from the choice of membrane material, the device preparation is identical to the procedure used for GO nanofluidic devices. In order to fabricate the membrane-based nanofluidic devices, membranes were cut into rectangular pieces and immersed in a de-gassed blend of polydimethylsiloxane (PDMS) prepolymer and curing agent. Samples were cured overnight at 60°C. After curing, two reservoirs were carved out in the PDMS device in order to expose the two ends of the membrane to the electrolyte solutions.

Conductivity measurement of the nanofluidic devices. Two Ag/AgCl electrodes were inserted into both the source and drain reservoirs to measure proton current through the membranes. The representative $I-V$ curves of the membrane based nanofluidic devices were recorded at different HCl concentrations, ranging from 10^{-6} M to 1 M. The conductivity was calculated based on the measured physical dimensions of the membranes and the interlayer spacing. XRD results suggest that the interlayer space is fully hydrated, and corresponds to about 34% of the total thickness of

the thin film. Therefore, for the calculations of channel conductivity, the collective channel thickness of the films was taken as 34% of the membrane thickness determined by profilometry and confirmed by cross-sectional SEM.

Measurement of surface charge density by ionic exchange. The surface charge density of a dry vermiculite film was determined by an ionic exchange method. An as-prepared vermiculite membrane was oven dried until the –OH band at 3200-3400 cm^{-1} was absent from the FTIR spectrum, indicating complete removal of water. Next 100 mg of dried membrane was soaked in 2 ml of 1 mM HCl overnight. The conductivity change in solution conductivity of the supernatant was used to infer the amount of H^+ that had been replaced by released interlayer Li^+, which can be used to calculate surface charge density. The supernatant was cast onto a Si wafer and dried. The presence of LiCl was confirmed by XPS measurements.

Effects of temperature and isotope on conductivity. In order to study temperature effects on ionic current, a nanofluidic device was made by implanting a thermometer into a PDMS block along with the vermiculite membrane. The ends of the membrane were exposed to 10^{-4} M HCl solution through the carved reservoirs. The acid soaked device was then immersed into an oil bath which was heated at a rate of 0.2°C per minute from room temperature to 80°C. At regular intervals, the ionic conductance was recorded by measuring I-V curves, while the temperature was measured by the embedded thermometer. For isotope effect measurements, vermiculite nanofluidic devices were soaked alternately in H_2O and D_2O solvent for extended time (~ 24 hours), to ensure complete hydration. After conductance was measured at particular solvent, devices were dried at 75°C in air for 24 hours before switching solvents.

Thermal stability of vermiculite nanochannels. The vermiculite membranes were placed on glass slides and heated in a muffle furnace at 200°C and 500°C in air for a day. To avoid exfoliation and complete disintegration of the membrane in water,[110] rehydration was done by adding a small aliquot of water that was just enough to cover the glass supported membrane. XRD pattern was then acquired on the water covered membrane after soaking overnight.

CHAPTER 5

KIRIGAMI NANOFLUIDICS

We have seen that GO paper and VMT paper satisfy some of the essential requirements of a nanofluidic channel array material. Both materials contain water-filled channels of uniform nanoscale width, through which unipolar ionic transport and surface-charge-governed conductivity can be observed. Due to the exceptionally narrow channel width of both 2D nanofluidic papers, the onset concentration of these nanofluidic transport properties is a relatively high value of ~10^{-2} M. What remains to be proven is whether these new 2D nanofluidic materials can indeed be used as a platform for assembling nanofluidic devices. In this chapter, we will explore the use of our 2D nanofluidic materials to construct simple ionic analogues to semiconductor devices.

Nanofluidic channels are conceptually analogous to extrinsically doped semiconductors in the sense that they permit unipolar transport with tunable carrier density and sign. Semiconductor doping, of course, has enabled a wide variety of electronic devices and circuits with a tremendous

impact on everyday life. Nanofluidic research has apparently taken inspiration from the successes of semiconductor device research, as nanofluidic systems have been extensively employed to demonstrate similar devices using ions as charge carriers. For example, nanofluidic channels have recently been used to demonstrate ionic rectifiers,[119-121] p-n junctions,[114, 122-123] field-effect transistors,[91, 124] and logic gates.[125] Diodes, one of the most basic types of semiconductor device, have been a particularly appealing model system for nanofluidic studies. Since ion transport through the nanochannels is strongly regulated by the interplay between surface charge, Debye length, and channel dimensions, ionic current rectification can be achieved by breaking the symmetry of these parameters at the two terminals of the nanochannels. One occasion where symmetric nanochannels may exhibit asymmetric transport characteristics is if the electrolyte concentrations at the source and drain reservoirs are different.[126-127] A more common strategy is to fabricate nanochannels with asymmetric sizes and inner surface properties.[119-121] This strategy is effective, but it typically relies on extensive use of lithography and therefore is inaccessible to many would-be researchers. And, the 10-nm-scale channel height requires very low electrolyte concentrations to be reached before the Debye layers of opposing walls are large enough to overlap.

By now you are aware that reconstructed layered membranes offer a solution to these problems. Exfoliated thin sheets such as GO or clay can be restacked *en masse* to create a membrane with a high volume fraction of interconnected 2D nanochannels. Compared to other nanofluidic systems, this method of channel fabrication is inexpensive, scalable, and requires relatively little equipment. While the range of channel spacing available is unfortunately limited to the natural interlayer spacings of the materials (with some exceptions[128]), the channel spacing

is consistent throughout the film and is robust to manhandling. Since it is this channel height that is responsible for the confinement of the electrolyte, the nanofluidic ionic transport properties are maintained regardless of the lateral dimensions or shape of the 2D nanochannel network. The material can be cut, twisted, and folded without altering the spacing. I have said that the development of 2D nanofluidics will enable studies that would be prohibitively expensive or unwieldly in other nanofluidic platforms; by allowing cuts and other deformations, the 2D nanofluidic platform enables some studies that are impossible in other nanofluidic systems.

In this chapter I aim to demonstrate that the 2D nanofluidic material platform can be used to create diodes and other devices of the sort that were previous only available to lithographically-defined channels. This was first accomplished serendipitously, by naively trying an experiment that would have been silly and wasteful if it were tried on any other nanofluidic platform: GO paper was cut into various shapes to see how macroscopic shape might affect nanofluidic transport.

GO paper and nanofluidic devices are prepared as previously, but in different macroscopic shapes. All shapes are approximately 8 mm wide by 20 mm long. The working electrode (or source) is placed on the left side and the drain and reference are placed on the right. Illustration of the device setup is shown in Figure 5.1, and the resulting IV curves are shown in Figure 5.2. The I-V curve measured through a GO rectangle is Ohmic, and symmetric between positive and negative voltages (Figure 5.2a). However, a triangle or trapezoid shape gives ionic current rectification (ICR) (Figure 5.2b), with a forward current that is higher than the reverse current at a given voltage. ICR is only observed in the surface-charge-governed concentration regime.

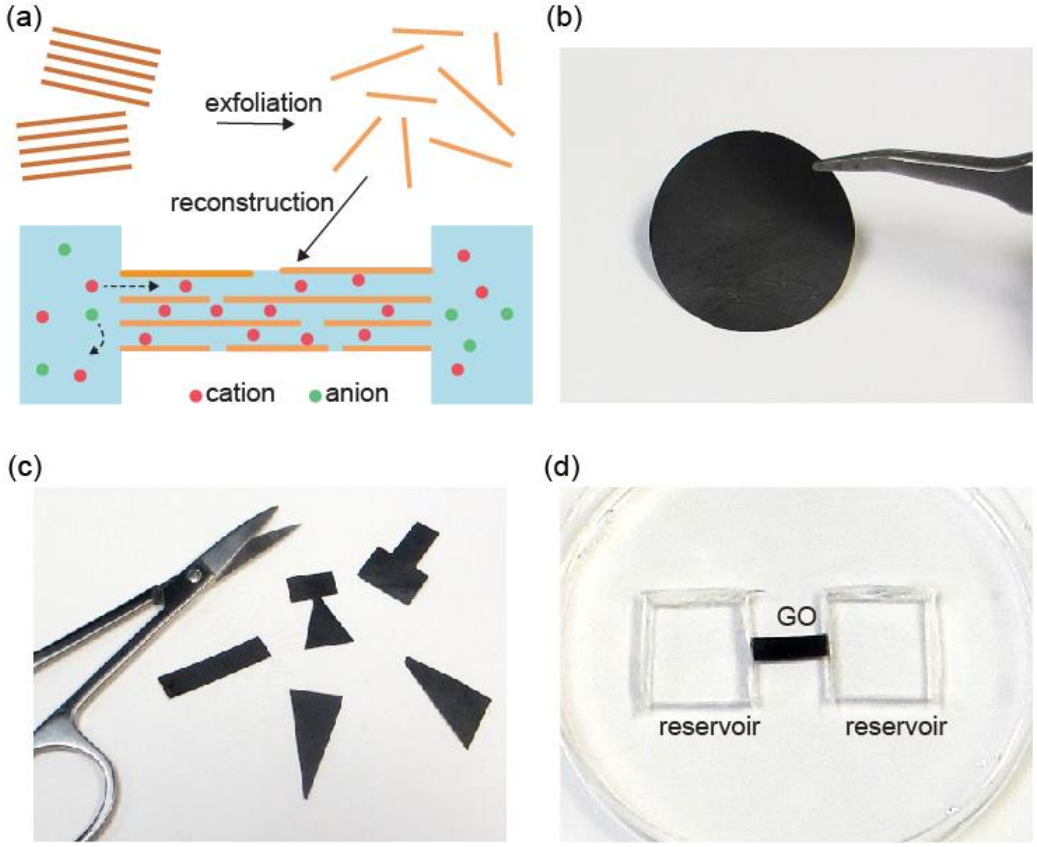

Figure 5.1. Lamellar "paper" as a platform for Kirigami nanofluidics. *(a) Schematic illustration of the synthesis and assembly of a 2D nanofluidic device. Exfoliated 2D sheets, such as GO, are reconstructed by restacking to form (b) a paper-like thin film with macroscopic dimensions. (c) Different device shapes can be tailor cut from the GO paper. (d) A GO strip is sealed in PDMS with both ends exposed to carved reservoirs for electrolytes.*

When the observation of shape-induced ICR was first reported,[129] we suggested that the narrowing of the GO paper cross-section in the forward direction caused carriers to flow in faster than they could flow out, leading to an enhanced carrier density inside the channels and thus higher conductivity; meanwhile, the widening of the GO paper in the reverse direction caused carriers to pour out faster than they were replenished, leading to depletion. Such a mechanism, which I will call the "bottleneck" mechanism, has successfully explained rectification in other nanofluidic systems, such as conical-shaped pores. It was later realized that this explanation conflicts with

what we already know about GO paper. Unlike many other systems, GO paper has a permselectivity of 1 throughout the entire macroscopic channel length. Without a mobile balancing charge, any depletion of the anions over a large distance must create a massive space charge. Yet the applied field is relatively small – a 0.1 V drop over a distance of 1 cm is enough to produce rectified ionic current – so the carrier concentration inside surface-charge-governed GO paper must match the surface charge density. The electric field applied in this experiment is far too small to create such a large space charge.

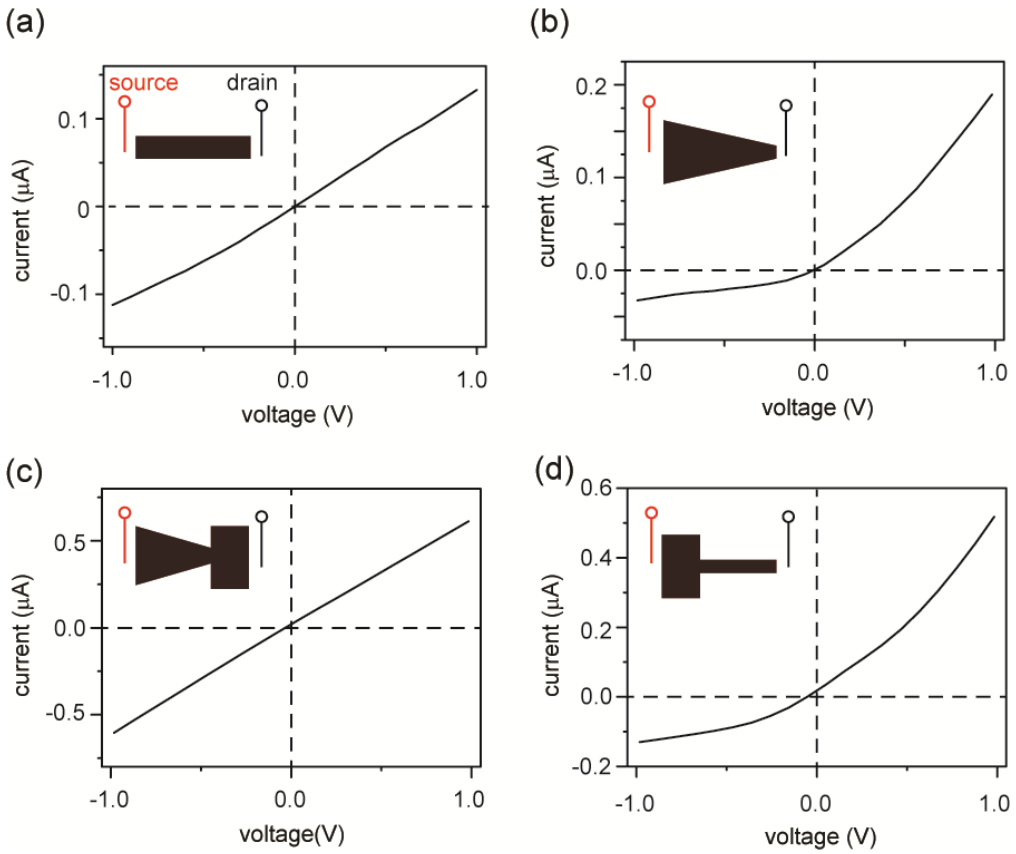

Figure 5.2. Kirigami nanofluidic devices. *(a) A rectangular piece of GO paper shows symmetric current under both forward and reverse bias. (b) When cut into a trapezoidal shape, the device rectifies the current, exhibiting typical diode-like behavior. (c) A piece of GO paper with the shape of a "diode sign" does not show rectifying behavior. (d) A T-shaped GO paper shows a diode-like rectifying current. The insets illustrate the top view of the GO papers. For consistency, the left reservoirs of all devices are designated as the source. These results suggest that current rectification is only determined by the relative widths of the two ends, and not by the shape of the GO paper in between.*

Furthermore, two other shapes were found to behave differently than the bottleneck mechanism predicts. A "diode-sign" shape, consisting of a trapezoid with a broad thin base appended to the drain side, would be expected to rectify according to the proposed mechanism, since its interior geometry resembles the trapezoid. Instead the experimental I-V curve is Ohmic, as shown in Figure 5.2c. Meanwhile, a "T" shape would be expected to show relatively little rectification, since its interior resembles a rectangle for most of its length. Instead this shape rectifies just as much as a trapezoid, as shown in Figure 5.2d. When all four of these shapes were considered together, the presence or absence of ICR appears to be determined simply by the relative sizes of the two exposed edges. When the edge lengths match, a linear I-V curve is obtained, but when the edge lengths are different, ICR is observed. Seeing as shapes with similarly-sized ends give Ohmic conductivity, and shapes with asymmetric ends give rectification, regardless of their interior symmetry, we begin to suspect that it is the area around the GO-reservoir interfaces that determines whether rectification will occur.

In a prior study of nanofluidic channels by Yossifson *et al*, ionic current rectification was achieved by a mechanism that seems to describe what we have observed here so far. Yossifson predicted that concentration polarization effects would lead to depletion and enrichment of charge carriers at the inlet and outlet of a nanochannel respectively.[130] When they created a T-shaped nanochannel with asymmetric inlet and outlet sizes, they were able to observe different conductance in different directions, depending on whether the highly resistive depletion zone fell on the narrow or wide end of the channel.[131] Yossifson's model does not fully describe the GO paper system – notably, GO paper rectifies at all voltages, while rectification in the other system is only observed at high voltage – but, the underlying idea is highly relevant.

Selective transport of ions or molecules through a medium results in the development of concentration gradients near the inlet and outlet of the medium, a phenomenon termed *concentration polarization* (CP). The species favored for transport through the medium will become depleted near the inlet, as it is swept away through the medium faster than it can be replenished; likewise, that species becomes concentrated near the outlet. Meanwhile, the reverse is observed for the species whose transport is disfavored. Applied towards ionic transport through a cation-selective membrane, CP leads to the depletion of *both* cations and anions near the higher-potential end of the membrane, and the enrichment of *both* near the lower-potential end. If a membrane has asymmetric interfacial areas, and the interfacial resistance is greater than the resistance of the membrane itself, then this effect is sufficient to generate ICR.

Figure 5.3a qualitatively illustrates how CP at the interfaces of a trapezoidal GO paper can lead to ICR. The total ionic resistance of the system consists of five terms in series: the two reservoirs, the two channels–reservoir interfaces (*i.e.*, CP zones), and the lamellar nanochannels themselves. The resistance of each section is inversely related to its width and its carrier concentration. The reservoirs are huge compared to other components, so their resistances are insignificant. The resistance of the GO nanochannel network is also relatively small, and is constant since the carrier concentration in the channels is fixed by the GO surface charge. Since the CP effect on the downstream side leads to the enrichment of ions, the resistance of the downstream interface becomes relatively insignificant. Ions are depleted on the upstream interface, however, and at this location the resistance becomes exceedingly high due to lack to charge carriers. Even though the interfacial CP zone is much shorter than the channel length, its resistance can be larger due to an orders-of-magnitude difference in carrier concentration. For shapes with

symmetric source and drain the sum of the resistances would be unchanged between forward and reverse bias. However, for shapes with asymmetric end sizes, such as the trapezoid, the wider edge is upstream under forward bias (Figure 5.3a, left) while the narrower edge is upstream under reverse bias (Figure 5.3a, right). Since resistance is inversely related to cross-sectional area, the CP zone resistance at the depleted narrow edge is larger than that at the depleted wide edge, and the forward current is higher than the reverse current.

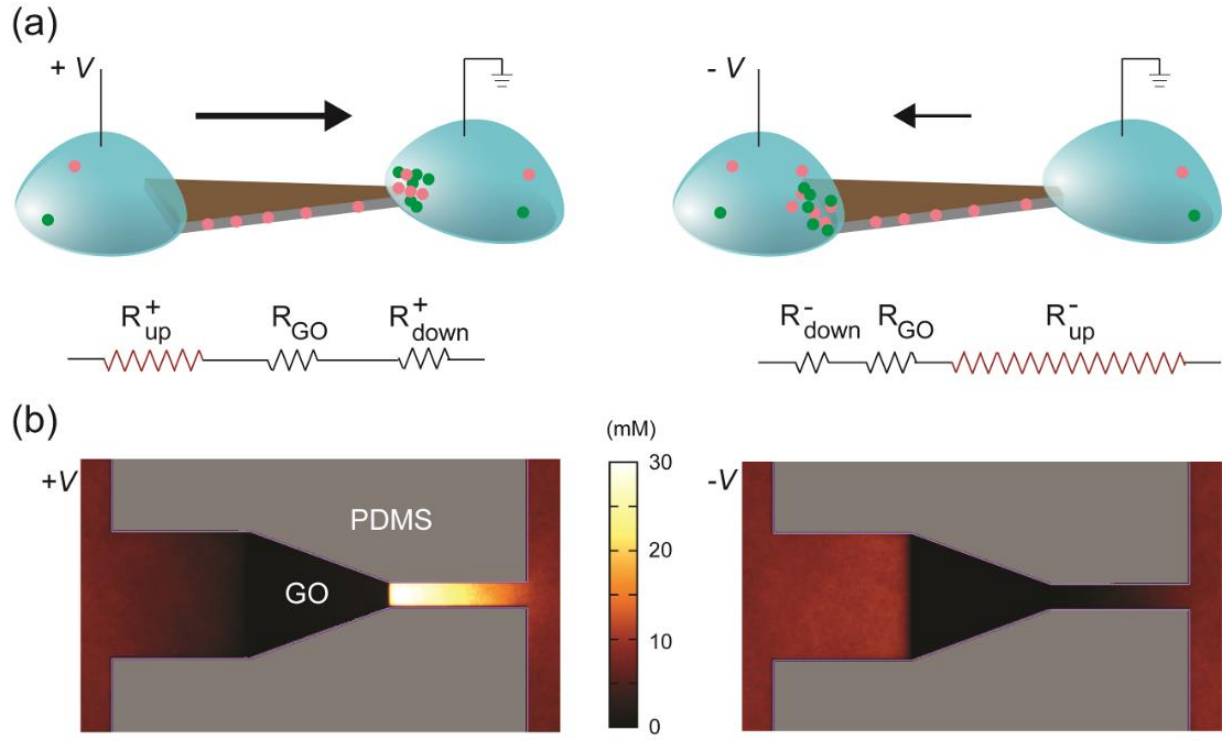

Figure 5.3. Rectification mechanism. *(a) Due to CP, ions are depleted at the upstream interface, leading to high upstream resistance R_{up}. On the other hand, the resistance at the downstream interface (R_{down}), where ions are enriched, is relatively insignificant. The resistance through the GO channels (R_{GO}) is constant. Under forward bias (+V), the upstream side is located on the left, which has larger width and thus lower R_{up}. Under reverse bias (–V), the upstream interface is on the right, which has narrower width and larger R_{up}. This explains current rectification in the trapezoidally shaped device. (b) Anionic concentration profile obtained in molecular dynamics simulations of the trapezoidal GO film and its reservoirs. Note the clear difference in the ionic concentration profile between forward (left) and reverse (right) bias, in agreement with Figure 5.3a. To accurately capture the quasi-one-dimensional shape of the CP zones in the experimental device, two artificial "channels" are added at the two ends in simulation.*

Quantitative illustration of this effect can be seen in a molecular dynamics simulation of this system carried out by our colleagues Beckerman and Luijten, which confirm the existence of CP regions that dominate the overall resistance of the system. In these simulations, a GO nanochannel network is immersed in an electrolyte consisting of explicit ions and implicit solvent, and the system is allowed to reach steady state under an applied voltage bias (see Methods). The ion concentration shows asymmetric CP under forward and reverse biases (Figure 5.3b) in qualitative agreement with Figure 5.3a, leading to asymmetric ionic current upon voltage reversal. The relationship between the rectification ratio and the geometrical asymmetry is consistent between simulation and experiment, and supports the proposed mechanism. Note that as far as this mechanism is concerned, the channel conductance, depletion-zone length, ion concentrations, and system size are only important in relation to one another, and therefore the differences of these values between simulation and experiment can be ignored. Also note that while the spatial extent of the CP zone is a healthy fraction of the simulation size, it would be tiny in comparison to the thickness of an actual GO paper device. As such, while the concentration gradient would extend out radially from the interface in simulation, it would effectively be 1-dimensional in the actual device. Therefore, walls were added immediately abutting the GO paper, so that the simulation would accurately reproduce the 1D concentration gradient of the device.

The dimensionality of the CP zone is apparently responsible for the differences between the rectification observed here and that observed in the prior work by Yossifon.[130-131] A radially-symmetric CP zone, such as the one Yossifon's single-layer device created, has a field-focusing effect that confines depletion to a very small area,[130] and as such the interface has a relatively small effect on the system resistance. The CP zone will only grow to an appreciable spatial extent when

ions are depleted all the way down to a concentration of zero, and rectification will not be observed until then. Yossifon indeed notes that there are different regimes in the IV curve, corresponding to partial depletion, full depletion, and beyond that an overlimiting vortex instability; in the diode test,[131] Yossifon only sees rectification in the latter two regimes. Rectification does not show up until fields of 100 V cm^{-1}. However, our device contains thousands of lateral channels in a microns-thick stack, which is far thicker than the CP zone and creates a 1-dimensional concentration gradient in the CP zones. As Yossifon noted,[130] the 1-dimensional expression for concentration polarization is exempt from this field-focusing effect. Thus, the CP depletion zone resistance in our system at low voltage can be a much greater portion of the system resistance than it would be in the single-layer system, allowing us to observe rectification at voltages as low as 0.1 V cm^{-1} (see Figure 5.2). The lower voltage demand could prove to be a crucial advantage of the 2D nanofluidic membrane system over the other CP rectifier system.

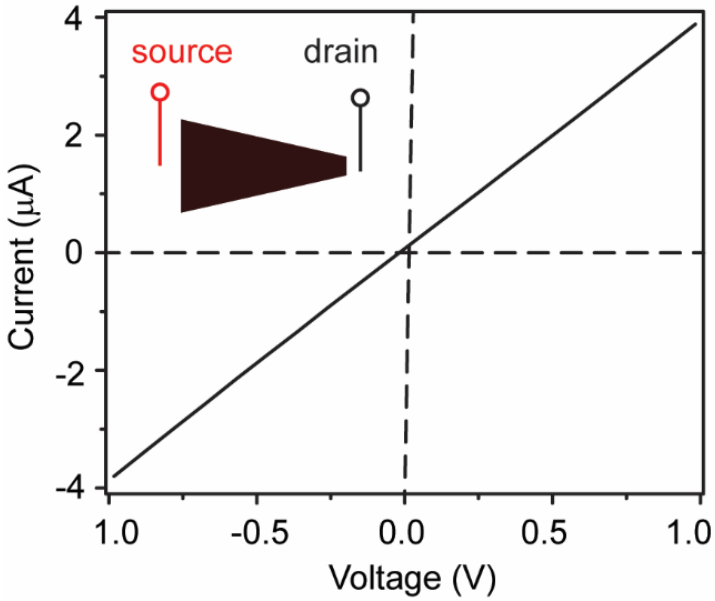

Figure 5.4. No current rectification when the channels are no longer charge selective. *At high electrolyte concentration, where the Debye layer is screened by electrolyte, the channels lose their charge selectivity. The CP mechanism predicts rectification will be lost in this circumstance. Indeed, a trapezoid GO device loses its diode-like property when KCl concentration is 50 mM.*

The present hypothesis, that CP zone resistance dictates rectification, can be tested by several device experiments (and fortunately, device fabrication is inexpensive in our system). First, since CP is caused by *selective* ion transport, rectification should disappear in the bulk conductivity regime. It does (Figure 5.4). Second, the direction rectification should be reversed if the sign of the charge carrier is reversed. An anionic current would deplete carriers from the narrow interface if current is carried in the direction we have designated as forward, and from the wide end in reverse current. A cation-excluding membrane is created by noncovalently complexing GO with a polycation, poly(dimethyldiallylammonium chloride), before vacuum filtration. As seen in Figure 5.5, the use of this membrane indeed leads to a reversal of the diode direction. Lastly, the present hypothesis implies that rectification can be induced in a symmetrically-shaped membrane if the CP zones at the membrane interfaces are somehow made asymmetric. This might be achieved by giving the reservoirs different viscosities or different temperatures. Figure 5.6 shows that this can be achieved even more easily, by stirring one reservoir while leaving the other unstirred. A depletion zone cannot build up in the stirred side the way it can in the unstirred side; therefore, conductivity is higher when the stirred side is upstream than when the stirred side is downstream. A third means of creating asymmetry in the CP zones of a symmetric membrane was shown in another recent work, where the second half of a single-direction I-V scan showed a saturation-like plateau in ionic conductivity, less conductive than the first half, regardless of the scan direction.[132] The scan speed was not reported, but this observation might imply that the rectification seen in this case was a transient effect, and that the CP zones did not have time to relax to their steady state values during this voltage sweep.

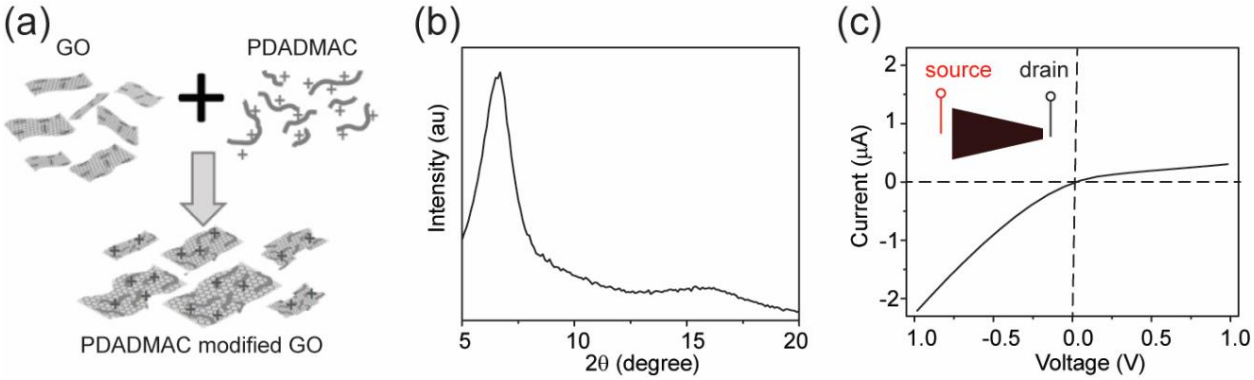

Figure 5.5. Rectification direction is reversed when surface charge is reversed. *(a) GO sheets (1 mg/mL in water) are modified with positively charged poly(diallyldimethylammonium chloride) (PDADMAC, 1 mg/mL in water), a positively charged electrolyte. (b) XRD pattern of PDADMAC-modified GO film in dry state. The d-spacing is 1.3 nm, larger than that of GO. (c) I–V curve recorded through a trapezoid nanofluidic device made from PDADMAC-modified GO film, showing that the rectification direction is reversed.*

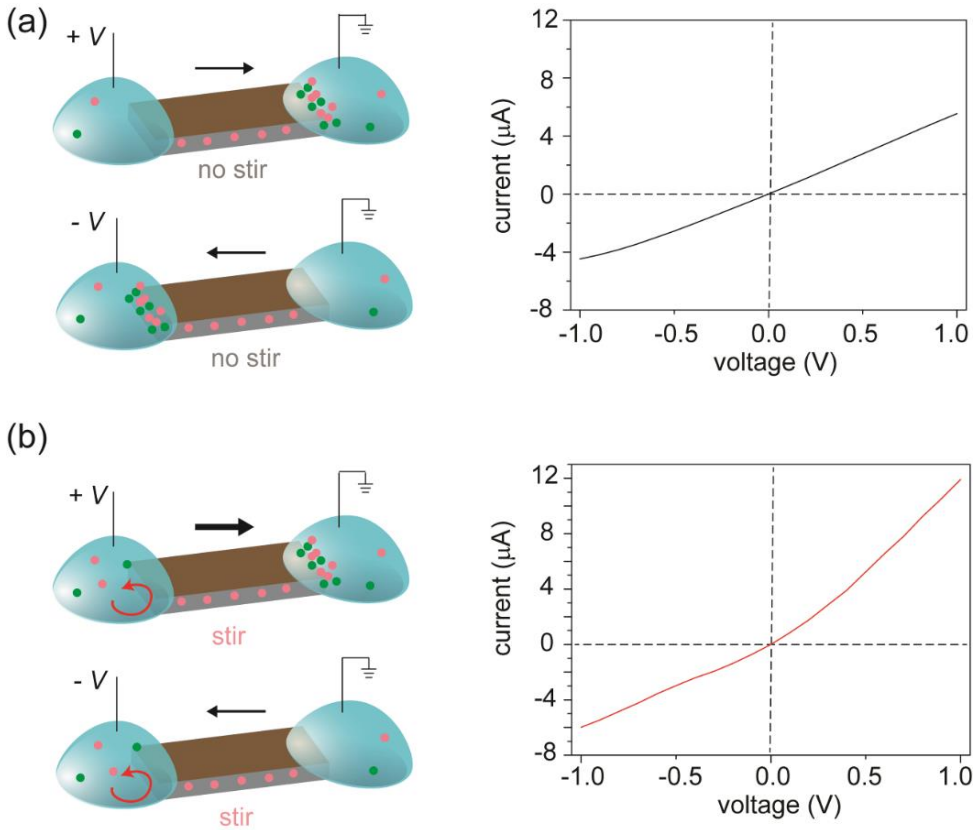

Figure 5.6. Disrupting CP zones by stirring. *(a) For a rectangular GO strip, the CP zones are symmetric under both biases leading to a symmetric I–V curve. (b) Stirring the left reservoir selectively suppresses the formation of CP resulting in current rectification.*

In order to estimate the relative contributions of the interfacial and channel resistances, the resistance is measured as a function of channel length in Figure 5.7. A rectangular GO strip was embedded in PDMS on a glass microscope slide. Between each measurement, a slice of the GO channel was removed by razor blade, and the length was measured with calipers. For channel lengths less than 5 mm, a precipitous drop in resistance is seen, perhaps due to leakage current from delamination of the PDMS from the GO channel. Extrapolation to length of 0 gives a crude estimate of the interfacial resistance, 350 kΩ. For sufficiently small devices, the total resistance is dominated by the resistance of the channel–reservoir interface on the upstream side. We can estimate that the interfacial resistance dominates for devices with channel length of 50 mm and below.

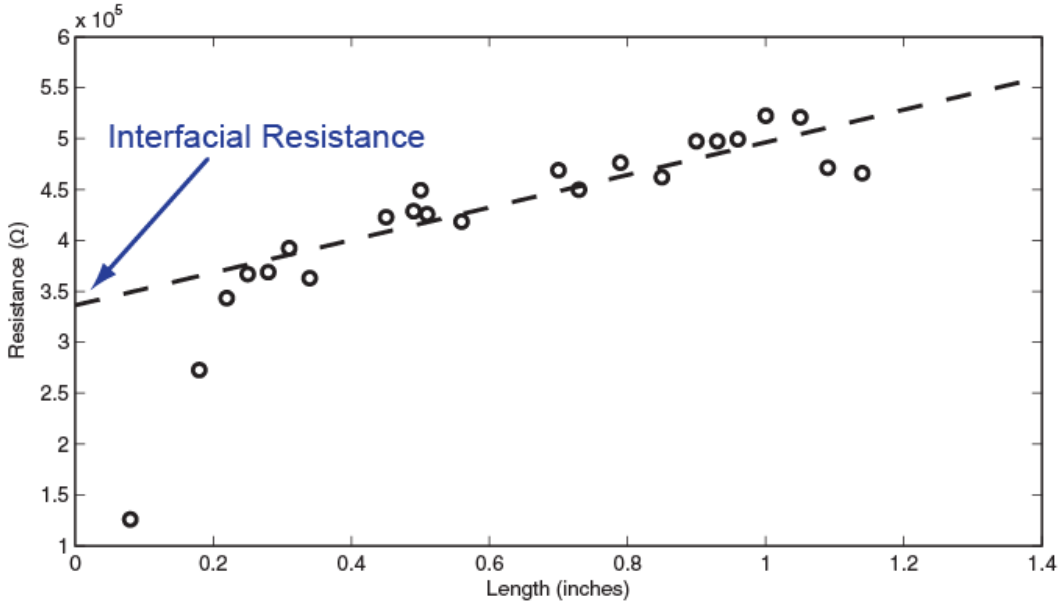

Figure 5.7. Estimating the channel-reservoir interfacial resistance. *A GO nanofluidic membrane was mounted on a glass slide and its conductivity measured. After each measurement, the device was shortened via razor blade, and allowed to equilibrate with 10^{-6} M KCl for 5 minutes before testing again. By plotting resistance as a function of length, fitting, and extrapolating to 0, we obtain an estimate of the interfacial resistance. The interfacial resistance is found to be the most dominant resistance of the system.*

Maximal rectification would be achieved if the CP depletion zone were the sole resistance in the system. The current through the system determines the degree of depletion, which determines the depleted zone resistance, which determines the current through the system; the negative feedback loop generated this way ensures that for any given voltage, the *conductivity* of the depleted zone approaches a constant value. In this ideal case, the system converge to a rectification ratio equal to the area ratio of the two ends. To the extent that the experimental device follows this ideal behavior, the rectification ratio can be quantitatively controlled by altering the ratio of the two interfaces' sizes. Figure 5.8 shows that for trapezoid-shaped GO paper devices, the rectification ratio is close to the edge width ratio, both in experiment and molecular dynamics simulation. Similarly, a device with multiple similarly-sized arms on the source side can be repeatedly switched between rectification ratios by connecting or disconnecting arms from the circuit; the rectification ratio is nearly equal to the number of arms connected to the circuit (Figure 5.9). Note that the reverse current is consistent, since it is dictated by the drain side. Only the forward current is affected by the number of arms connected to the source side of the device.

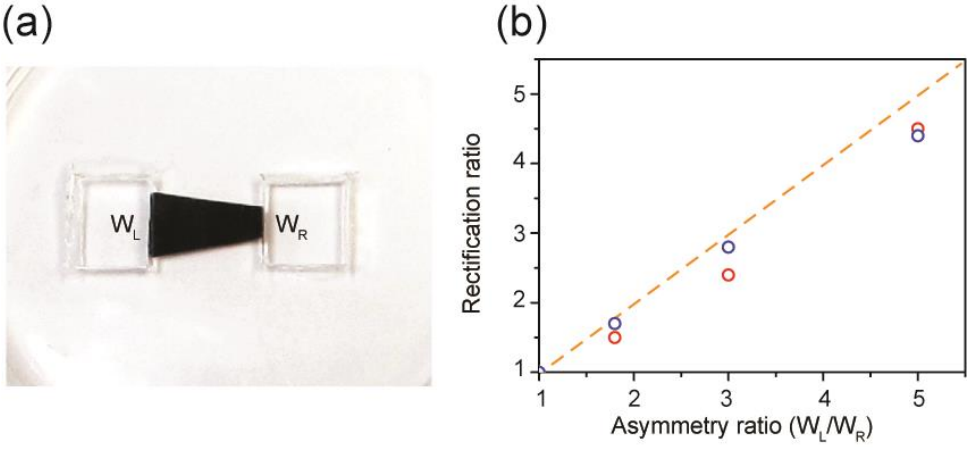

Figure 5.8. Rectification ratio determined by the asymmetry ratio of edge widths. *(a) A trapezoidal GO device with left-side width W_L and right-side width W_R. If the membrane resistance is neglected, then rectification ratio is expected to equal asymmetry ratio. (b) The measured (red circles) and simulated (blue circles) rectification ratios are close to the asymmetry ratio (W_L/W_R). The orange dashed line is an eye guide representing rectification ratio = W_L/W_R.*

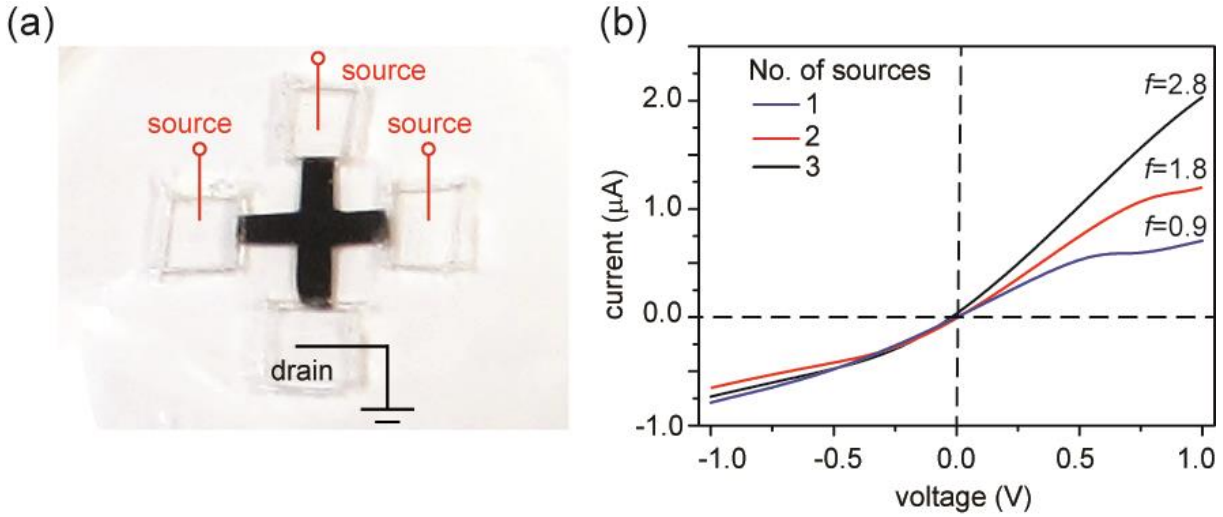

Figure 5.9. Programming the rectification ratio. *(a) Photo showing a cross-shaped GO paper with four branches. One branch is designated as the drain. By varying the number of branches that are connected to the source, the rectification ratio f can be tuned. (b) Current–voltage measurements show that the forward current varies in direct proportion to the number of source branches used. The reverse-voltage resistance is determined mostly by the edge length of the drain end and therefore remains largely unchanged.*

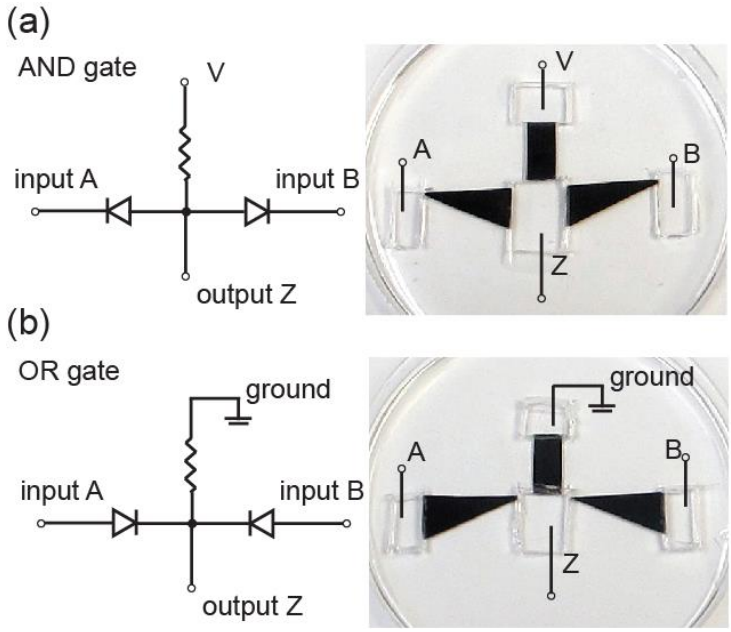

input A	input B	output Z	logic Z
1	1	3.9±0.1 V	1
1	0	0.7±0.2 V	0
0	1	0.6±0.2 V	0
0	0	0.5±0.1 V	0

input A	input B	output Z	logic Z
1	1	2.0±0.1 V	1
1	0	1.4±0.1 V	1
0	1	1.5±0.2 V	1
0	0	0.0±0.1 V	0

Figure 5.10. Ionic logic circuits. *(a) and (b) show, from left to right, the circuit diagrams, device photos, and truth tables of the AND and OR logic gates, respectively. The input high and low voltages are 4 V and 0 V, respectively. For both devices, a clear difference between logical 1 and 0 states is observed.*

Lastly, note that the devices shown here are modular and can be combined into larger circuits, provided the CP zones are unperturbed by the combination. To demonstrate, diode logic gates are assembled and tested (Figure 5.10). A significant and easily-distinguishable difference between the logical 1 and 0 states is observed, and the logic values agree with the corresponding logic algorithms. These elementary forms of logic circuits serve to illustrate the possibility of assembling kirigami-made nanofluidic elements together into larger circuits. Unfortunately, a considerable voltage across the device is observed, as is typical of diode logic gates. Refinement of this system can improve the efficiency to some extent, but in order to assemble logic gates that are efficient enough for even rudimentary ionic computing, we would have to develop a transistor-based logic gate.

In summary, this chapter offered one simple demonstration that the 2D nanofluidic platform can offer ionic analogues to semiconductor devices. An ionic diode was constructed by cutting a nanofluidic membrane into an asymmetric shape. The diode was shown to function by a concentration-polarization based mechanism. This is the second such CP-based rectifier demonstrated to date; unlike the first, this device rectifies current at very low applied fields, as low as 0.1 V cm^{-1} (compared to 100 V cm^{-1} previously). The performance difference arises from the multilayer geometry of the new device, which alters the shape of the CP zone and eliminates the field focusing effect. Our approach exploits the simplicity of fabrication enabled by the 2D nanofluidics platform, and the stable, uniform nanoscopic height of the channels. The operating voltage of this device is more practical for application, and the device's facile and inexpensive construction is expected to enable and accelerate future research in the domain of nanofluidics.

Methods

GO is fabricated *via* modified Hummer's method[5] and then purified *via* two-step washing as reported previously.[133] Vacuum filtration or the drop-cast method is used to obtain GO paper. The GO paper is typically 10 to 20 μm thick. Prior to embedding in PDMS precursor, the GO papers are cut into different shapes using scissors. Subsequently, the PDMS is cured at 70°C for 1 h and then two electrolyte reservoirs are carved out to expose the two ends of the GO film. The cut GO films have a length of about 1.5 cm. The fabricated device is then immersed in deionized water overnight to ensure complete hydration. Before ionic current measurement, the device is further immersed in testing electrolyte for at least 8 h to ensure stable conductance. Here the testing electrolyte is KCl at bulk concentration 10^{-4} M in water unless specified otherwise. Ionic current is recorded by a Keithley 2601A source meter with two Ag/AgCl electrodes. Ag/AgCl electrodes were tested before each experiment, by placing both electrodes in one reservoir and recording IV curves, and only used for experiments when the curve was Ohmic. For device tests, the scan speed was typically between 10^{-3} and 10^{-5} V s^{-1}. At faster scan speeds hysteresis was observed, and at slower scan speeds enough ions could pass through the device to alter the reservoir concentrations. For logic circuits, a Keithley 2400 source meter is used to provide input voltages. More details regarding device fabrication and measurement can be found in the original report of 2D nanofluidic membrane fabrication.[134]

Molecular dynamics simulations by Beckerman are performed of ions in confined geometries, embedded in an implicit solvent. The ions are placed in a periodically replicated 350 nm × 200 nm × 4.98 nm simulation box. The length of the box is divided into a 50 nm bulk region, a 100 nm GO region, and two 100-nm-long "channel" regions that connect the GO to the bulk,

which are the widths of the GO–reservoir interfaces (Figure 5.3b). These channel regions were required to prohibit radial focusing[131] and therefore capture the quasi one-dimensional geometry that emerges at the interface of thousands of stacked nanochannels. The external field is applied along the *x*-direction. A set of repulsive walls represents the PDMS barricades and restricts ions from crossing the box boundaries in the *y*- and *z*-directions. The excluded volume of the GO sheets is modeled by a set of parallel, repulsive planes that are normal to the *z*-axis and separated by 1.66 nm in the *z*-direction. The surface charge of GO is modeled by embedding monovalent charges at a surface density of 0.046 e^{-}/nm^2, near the upper range for GO.[97] The area of the GO trapezoid is kept at a constant 11,000 nm^2 for all geometric asymmetries. Simulations were performed with the bulk concentration fixed at 7.6 mM.

CHAPTER 6

CONCLUSIONS

In this concluding segment, I wish to highlight interesting ramifications of the results presented so far, and speculate on what interesting findings may arise in future work. Let us review:

GO sheets exist in a high-aspect-ratio configuration in solution, no matter the solvation condition. This is implied by previous work on tethered membranes, and is shown explicitly by our own observations of optical birefringence in GO samples. This does not preclude the formation of smaller wrinkles (indeed, the methods used here wouldn't necessarily detect such wrinkles), only the wholesale crumpling of the sheet. If solvent conditions get bad, then GO sheets will prefer to stack up, as solid multi-sheet aggregates, rather than crumpling. Aggregated GO remains birefringent and orientationally ordered, even at the lower limit of experimentally accessible concentrations. While it's conceivable that a crumple can be thermodynamically stable, there is an

immense energy barrier preventing the sheets from spontaneously crumpling. This is implied by my work and established by the complementary work of collaborators.

I expect it would be unproductive to continue studying GO's solution configuration using the methods presented here. The absence of spontaneous solvent induced crumpling has been established for GO, and by extension we can safely conclude that other 2D materials, which are stiffer than GO and have weaker self-adhesion, will not crumple either. The ease with which clays and other 2D materials form liquid crystal phases supports this conjecture as well. Apart from an instance of MoS_2 crumples forming during air-drying of a TEM sample,[135] there are very few reports of inorganic 2D materials forming crumpled or wrinkled phases.

That said, there are conformation transformations other than crumpling which may find technological relevance. For instance, a sheet which is flat on long length scales can still develop shorter-scale wrinkles, buckles and fluctuations, which might affect the electronic properties or solvent-accessible surface area of the sheet.[136-137] Unfortunately for us, such a transition would not change the aspect ratio of the sheet enough to bring about a distinct change in liquid crystallinity. Radiation scattering would be the best way to study this sort of wrinkling. Notably, two recent studies have applied scattering methods to study bending and fluctuation of GO sheets on the 10 nm length scale. One study finds that GO sheets contain extensive small wrinkles, which may affect the ability of GO sheets to transfer load from their polymer matrices in composites applications.[138] The other observes similar wrinkles, and uses mechanical testing with *in situ* SAXS to estimates the stiffness of the sheet towards those wrinkles.[139] SAXS is the most viable approach for trying to find a wrinkling transition in exfoliated 2D nanosheets. Birefringence is a

quick, easy, inexpensive measure of configuration, but it can only reliably detect massive differences in configuration, and will overlook subtler configurational changes such as wrinkling.

We now know, however, that when crumpling or collapse of an entire sheet is seen, the transition cannot be explained by the "intrinsic nature of graphene nanosheets, which result from the fact that the 2D membrane structure becomes thermodynamically stable via bending".[27] Some external force must act on the sheet in order to form a cGO ball. Drying effects are the most likely explanation.

Moving on, we also found that the spaces between two-dimensional nanosheets are two-dimensional galleries, atoms thick and microns wide. Hydration of this space creates a network of nanoscopic two-dimensional ion channels. This strategy is demonstrated for exfoliated vermiculite as well as graphene oxide. Ionic currents carried through these confined channels share many of the critical properties of lithographically-defined nanofluidic channels. Our "2D nanofluidic" ion channel array may thus circumvent the need for lithography in nanofluidics research. We also saw that new ionic device geometries can be made simply by cutting the membrane into different shapes. For instance, by cutting the membrane into a shape with anisotropic membrane-reservoir interfacial areas, we can create ionic diodes. The performance of this class of devices is mostly determined by concentration polarization effects at these interfaces.

The confinement felt by ions and water molecules in this system is far greater than that of other nanofluidic systems. In GO and vermiculite alike, the hydration channel is just a couple water molecules wide – by comparison, channels made by patterning, etching and bonding are typically 50-100 nm tall. Even carbon nanotube channels are far larger than ours. Detailed transport studies

in this extremely confined environment may produce interesting findings about the diffusion constants of water and ions. Ions may be found to experience friction-like effects as they are dragged through spaces barely larger than themselves. We might even ask whether the word *nanofluidic* is an appropriate descriptor of the "2D nanofluidic" system, since the network of water molecules inside our layers might be found to more closely resemble a solid than a fluid.

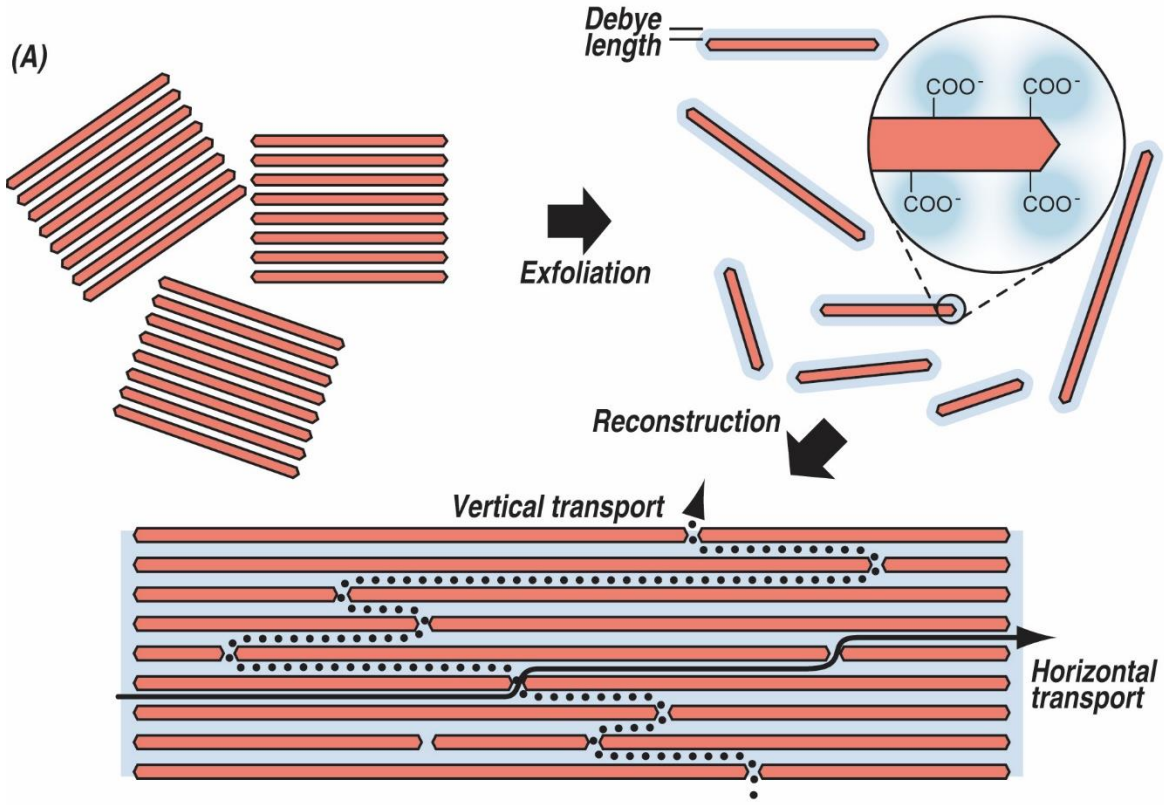

Figure 6.1 Schematic of 2D nanofluidic membrane assembly and cross-section. *Since assembly of 2D nanosheets aligns them in a horizontal orientation, the nanochannels between the sheets also lie horizontal. For ions to move vertically, they must therefore meander around nanosheets, slowing them down considerably. From A. Koltonow and J. Huang, "Two-dimensional Nanofluidics," Science, 351, 1395 (2016). Reprinted with permission from AAAS.*

One of the largest areas of application for ion-selective materials is as ion exchange membranes for applications such as fuel cells. The exfoliated vermiculite membrane, with its thermal and chemical resistance and high proton mobility, combines many properties that proton-

exchange membrane fuel cells demand. Unfortunately, the high proton mobility is only observed in the "in-plane", or horizontal, direction, while these membrane applications demand ion transport in the "cross-plane", or vertical, direction. In our system we find a difference on the order of 10^2 – 10^3 between horizontal and vertical mobilities. The reason for the differing mobilities is shown in Figure 6.1. Ions traveling horizontally are unimpeded by the nanochannel walls; however, ions traveling in the vertical direction must meander around horizontally oriented walls of aspect ratio >1000 to pass through the membrane. The difference in the path length gives rise to an apparent difference in ionic mobility. It follows from this mechanism that the vertical mobility can be enhanced by changing the nanostructure of the material. If the nanosheets that form the channel walls were oriented vertically, then vertical mobility would improve dramatically. This might be achieved by using some sort of self-assembly method. For instance, by coating a wafer with a ligand that specifically recognizes the edge groups of vermiculite sheets, immersing the wafer in exfoliated vermiculite solution, then using etching or transfer methods to remove the vermiculite attached to the surface, one might be able to make a membrane with vertically-oriented sheets. Alternately, surfactant-guided electrochemical deposition might be a useful way to synthesize vertically oriented films of other lamellar metal oxide sheets.[140-141] Such a membrane might also be reoriented manually, *e.g.* by folding and slicing the flexible vermiculite paper into jelly-roll pieces. Lastly, rather than reorienting the sheets, a simpler way to improve mobility is by decreasing the distance ions would need to meander. This might be achieved by etching pinholes into the nanosheet surface prior to vacuum filtration, or by simply using smaller sheets.

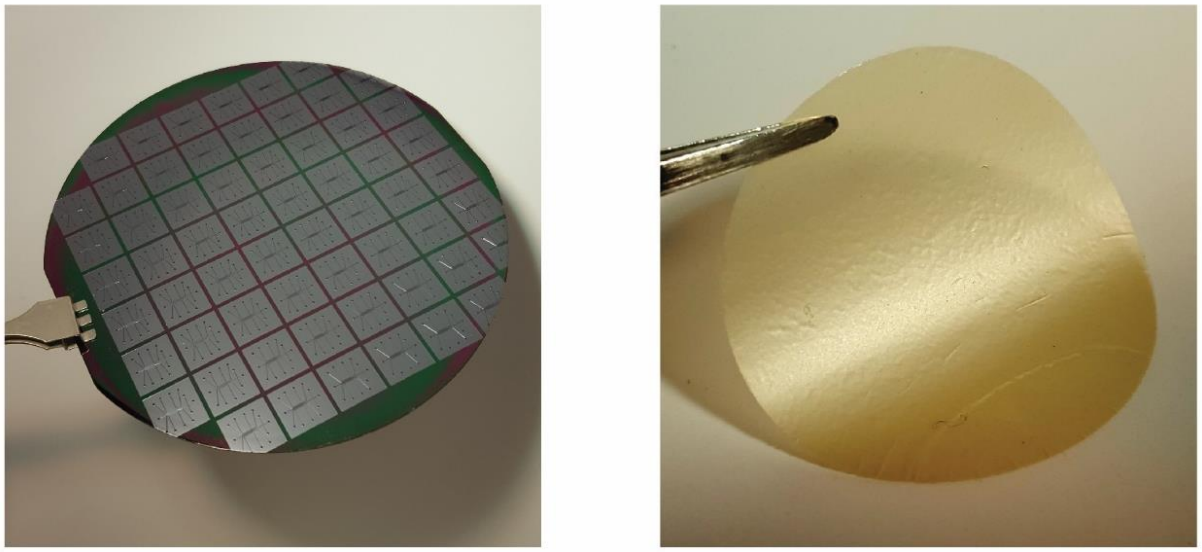

Figure 6.2. A doped semiconductor wafer (left) resembles a 2D nanofluidic membrane (right)*, in that they both have a planar geometry, with a single dominant charge carrier that moves in the plane of the top surface. New ionic devices might be inspired by previous achievements in integrated electronics.*

Lastly, we can draw an analogy between 2D nanofluidics and extrinsically doped semiconductor wafers, because they both have a planar geometry and only one type of dominating charge carriers (Figure 6.2). One can imagine using these lamellar films as "ionic wafers" to create integrated ionic circuitry. Gates, for instance, could be evaporated on top of the vermiculite membrane, allowing for switching between different carrier concentrations. Preliminary experiments were unable to obtain significant depletion of ions from the interior of a device, suggesting that new geometries might be needed to achieve gating in this system. Since a key advantage of the 2D nanofluidic platform is that it does not require lithography, we should seek non-lithographic strategies for imparting additional function. Preliminary findings in our lab show that cut pieces of GO paper can be attached together by using small amounts of water to solvent weld them together. By attaching p-type and n-type nanofluidic membranes together, we might assemble working p-n junctions and eventually transistors.

In this work, I strove for accessibility. When I could, I used inexpensive materials, widely available characterization methods, and I explained my findings in terms of scaling arguments and back-of-the-envelope calculations. I styled my work this way so that it could be understood, replicated, and improved upon by as many people as possible. Few universities offer the resources or the institutional advantages of Northwestern, and yet there are millions of brighter minds than mine. My hope, then, is that by taking nanofluidics out of the cleanroom and into the wet lab, I have given someone the means to pursue research that would have otherwise been unavailable to them. I hope to learn one day that this work has succeeded in inviting new researchers to the field.

REFERENCES

1. Novoselov, K. S.; Geim, A. K.; Morozov, S. V.; Jiang, D.; Zhang, Y.; Dubonos, S. V.; Grigorieva, I. V.; Firsov, A. A., Electric field effect in atomically thin carbon films. *Science* **2004,** *306* (5696), 666-669.

2. Lee, C.; Wei, X. D.; Kysar, J. W.; Hone, J., Measurement of the elastic properties and intrinsic strength of monolayer graphene. *Science* **2008,** *321* (5887), 385-388.

3. Griffith, A. A., The Phenomena of Rupture and Flow in Solids. *Philosophical Transactions of the Royal Society of London* **1920,** *221* (587), 163-198.

4. Brodie, B. C., On the Atomic Weight of Graphite. *Philosophical Transactions of the Royal Society of London* **1859,** *149*, 249-259.

5. Hummers, W. S.; Offeman, R. E., Preparation Of Graphitic Oxide. *Journal of the American Chemical Society* **1958,** *80* (6), 1339-1339.

6. Dikin, D. A.; Stankovich, S.; Zimney, E. J.; Piner, R. D.; Dommett, G. H. B.; Evmenenko, G.; Nguyen, S. T.; Ruoff, R. S., Preparation and characterization of graphene oxide paper. *Nature* **2007,** *448* (7152), 457-460.

7. Xu, Y. X.; Sheng, K. X.; Li, C.; Shi, G. Q., Self-Assembled Graphene Hydrogel via a One-Step Hydrothermal Process. *ACS Nano* **2010,** *4* (7), 4324-4330.

8. Shao, J. J.; Wu, S. D.; Zhang, S. B.; Lv, W.; Su, F. Y.; Yang, Q. H., Graphene oxide hydrogel at solid/liquid interface. *Chemical Communications* **2011,** *47* (20), 5771-5773.

9. Huang, X.; Yin, Z. Y.; Wu, S. X.; Qi, X. Y.; He, Q. Y.; Zhang, Q. C.; Yan, Q. Y.; Boey, F.; Zhang, H., Graphene-Based Materials: Synthesis, Characterization, Properties, and Applications. *Small* **2011,** *7* (14), 1876-1902.

10. Kim, J.; Cote, L. J.; Huang, J. X., Two Dimensional Soft Material: New Faces of Graphene Oxide. *Accounts of Chemical Research* **2012,** *45* (8), 1356-1364.

11. Hwa, T.; Kokufuta, E.; Tanaka, T., Conformation of Graphite Oxide Membranes In Solution. *Physical Review A* **1991,** *44* (4), R2235-R2238.

12. Wen, X.; Garland, C. W.; Hwa, T.; Kardar, M.; Kokufuta, E.; Li, Y.; Orkisz, M.; Tanaka, T., Crumpled and Collapsed Conformations In Graphite Oxide Membranes. *Nature* **1992,** *355* (6359), 426-428.

13. Kuilla, T.; Bhadra, S.; Yao, D. H.; Kim, N. H.; Bose, S.; Lee, J. H., Recent advances in graphene based polymer composites. *Progress in Polymer Science* **2010,** *35* (11), 1350-1375.

14. Kim, J.; Cote, L. J.; Kim, F.; Yuan, W.; Shull, K. R.; Huang, J. X., Graphene Oxide Sheets at Interfaces. *Journal of the American Chemical Society* **2010,** *132* (23), 8180-8186.

15. Kim, J.; Tung, V. C.; Huang, J. X., Water Processable Graphene Oxide: Single Walled Carbon Nanotube Composite as Anode Modifier for Polymer Solar Cells. *Advanced Energy Materials* **2011,** *1* (6), 1052-1057.

16. Tung, V. C.; Huang, J. H.; Tevis, I.; Kim, F.; Kim, J.; Chu, C. W.; Stupp, S. I.; Huang, J. X., Surfactant-Free Water-Processable Photoconductive All-Carbon Composite. *Journal of the American Chemical Society* **2011,** *133* (13), 4940-4947.

17. Cote, L. J.; Kim, F.; Huang, J. X., Langmuir-Blodgett Assembly of Graphite Oxide Single Layers. *Journal of the American Chemical Society* **2009,** *131* (3), 1043-1049.

18. Cote, L. J.; Kim, J.; Zhang, Z.; Sun, C.; Huang, J. X., Tunable assembly of graphene oxide surfactant sheets: wrinkles, overlaps and impacts on thin film properties. *Soft Matter* **2010,** *6* (24), 6096-6101.

19. Luo, J. Y.; Jang, H. D.; Sun, T.; Xiao, L.; He, Z.; Katsoulidis, A. P.; Kanatzidis, M. G.; Gibson, J. M.; Huang, J. X., Compression and Aggregation-Resistant Particles of Crumpled Soft Sheets. *ACS Nano* **2011,** *5* (11), 8943-8949.

20. Lobkovsky, A.; Gentges, S.; Li, H.; Morse, D.; Witten, T. A., Scaling Properties of Stretching Ridges in a Crumpled Elastic Sheet. *Science* **1995,** *270* (5241), 1482-1485.

21. Kim, J. E.; Han, T. H.; Lee, S. H.; Kim, J. Y.; Ahn, C. W.; Yun, J. M.; Kim, S. O., Graphene Oxide Liquid Crystals. *Angewandte Chemie - International Edition* **2011,** *50* (13), 3043-3047.

22. Xu, Z.; Sun, H. Y.; Zhao, X. L.; Gao, C., Ultrastrong Fibers Assembled from Giant Graphene Oxide Sheets. *Advanced Materials* **2013,** *25* (2), 188-193.

23. Xu, Z.; Zhang, Y.; Li, P. G.; Gao, C., Strong, Conductive, Lightweight, Neat Graphene Aerogel Fibers with Aligned Pores. *ACS Nano* **2012,** *6* (8), 7103-7113.

24. Yeh, C.-N.; Raidongia, K.; Shao, J.; Yang, Q.-H.; Huang, J., On the origin of the stability of graphene oxide membranes in water. *Nature Chemistry* **2015,** *7* (2), 166-170.

25. Jung, I.; Pelton, M.; Piner, R.; Dikin, D. A.; Stankovich, S.; Watcharotone, S.; Hausner, M.; Ruoff, R. S., Simple approach for high-contrast optical imaging and characterization of graphene-based sheets. *Nano Letters* **2007,** *7* (12), 3569-3575.

26. Kim, J.; Cote, L. J.; Kim, F.; Huang, J. X., Visualizing Graphene Based Sheets by Fluorescence Quenching Microscopy. *Journal of the American Chemical Society* **2010,** *132* (1), 260-267.

27. Wang, G. X.; Shen, X. P.; Yao, J.; Park, J., Graphene nanosheets for enhanced lithium storage in lithium ion batteries. *Carbon* **2009,** *47* (8), 2049-2053.

28. Liaros, N.; Aloukos, P.; Kolokithas-Ntoukas, A.; Bakandritsos, A.; Szabo, T.; Zboril, R.; Couris, S., Nonlinear Optical Properties and Broadband Optical Power Limiting Action of Graphene Oxide Colloids. *Journal of Physical Chemistry C* **2013,** *117* (13), 6842-6850.

29. Jiang, L.; Shen, X. P.; Wu, J. L.; Shen, K. C., Preparation and Characterization of Graphene/Poly(vinyl alcohol) Nanocomposites. *Journal of Applied Polymer Science* **2010,** *118* (1), 275-279.

30. Wang, H. B.; Zhang, C. J.; Liu, Z. H.; Wang, L.; Han, P. X.; Xu, H. X.; Zhang, K. J.; Dong, S. M.; Yao, J. H.; Cui, G. L., Nitrogen-doped graphene nanosheets with excellent lithium storage properties. *Journal of Materials Chemistry* **2011,** *21* (14), 5430-5434.

31. Wan, L. J.; Ren, Z. Y.; Wang, H.; Wang, G.; Tong, X.; Gao, S. H.; Bai, J. T., Graphene nanosheets based on controlled exfoliation process for enhanced lithium storage in lithium-ion battery. *Diamond and Related Materials* **2011,** *20* (5-6), 756-761.

32. Hsieh, C. T.; Liu, Y. Y.; Roy, A. K., Pulse electrodeposited Pd nanoclusters on graphene-based electrodes for proton exchange membrane fuel cells. *Electrochimica Acta* **2012,** *64*, 205-210.

33. Su, X. Q.; Wang, G.; Li, W. L.; Bai, J. B.; Wang, H., A simple method for preparing graphene nano-sheets at low temperature. *Advanced Powder Technology* **2013,** *24* (1), 317-323.

34. Zhu, K.; Li, X. R.; Wang, H. H.; Li, J. Y.; Fei, G. Q., Electrochemical and anti-corrosion behaviors of water dispersible graphene/acrylic modified alkyd resin latex composites coated carbon steel. *Journal of Applied Polymer Science* **2017,** *134* (11), 12.

35. Li, X. N.; Zhu, X.; Zhu, Y. C.; Yuan, Z. Q.; Si, L. L.; Qian, Y. T., Porous nitrogen-doped carbon vegetable-sponges with enhanced lithium storage performance. *Carbon* **2014,** *69*, 515-524.

36. Rubinstein, M.; Colby, R. H., *Polymer Physics*. Oxford University Press: **2003**.

37. de Gennes, P. G., *Scaling Concepts in Polymer Physics*. Cornell University Press: **1979**.

38. Young, R. J.; Lovell, P. A., *Introduction to Polymers, Third Edition*. Taylor & Francis: **2011**.

39. Kantor, Y.; Kardar, M.; Nelson, D. R., Statistical Mechanics of Tethered Surfaces. *Physical Review Letters* **1986,** *57* (7), 791-794.

40. Ledoussal, P.; Radzihovsky, L., Self-Consistent Theory Of Polymerized Membranes. *Physical Review Letters* **1992,** *69* (8), 1209-1212.

41. Zhang, Z.; Davis, H. T.; Kroll, D. M., Scaling Behavior Of Self-Avoiding Tethered Vesicles. *Physical Review E* **1993,** *48* (2), R651-R654.

42. Wiese, K. J.; David, F., New renormalization group results for scaling of self-avoiding tethered membranes. *Nuclear Physics B* **1997,** *487* (3), 529-632.

43. Mori, S.; Kawanishi, K.; Wadati, M., Dilute And Semidilute Solutions Of Randomly Polymerized Membranes. *Journal of the Physics Society of Japan.* **1995,** *64* (1), 64-77.

44. Munkel, C.; Heermann, D. W., Folding Transitions Of Self-Avoiding Membranes. *Physical Review Letters* **1995,** *75* (8), 1666-1669.

45. Popova, H.; Milchev, A., Structure, dynamics, and phase transitions of tethered membranes: A Monte Carlo simulation study. *Journal of Chemical Physics* **2007,** *127* (19), 194903.

46. Plischke, M.; Boal, D., Absence Of A Crumpling Transition In Strongly Self-Avoiding Tethered Membranes. *Physical Review A* **1988,** *38* (9), 4943-4945.

47. Nelson, D. R.; Radzihovsky, L., Polymerized Membranes With Quenched Random Internal Disorder. *Europhysics Letters* **1991,** *16* (1), 79-84.

48. Kantor, Y.; Kremer, K., Excluded-Volume Interactions In Tethered Membranes. *Physical Review E* **1993,** *48* (4), 2490-2497.

49. Kroll, D. M.; Gompper, G., Floppy Tethered Networks. *Journal de Physique I* **1993,** *3* (5), 1131-1140.

50. Bowick, M. J.; Catterall, S. M.; Falcioni, M.; Thorleifsson, G.; Anagnostopoulos, K. N., The flat phase of crystalline membranes. *Journal de Physique I* **1996,** *6* (10), 1321-1345.

51. Bowick, M. J.; Catterall, S. M.; Falcioni, M.; Thorleifsson, G.; Anagnostopoulos, K., The flat phase of fixed-connectivity membranes. *Nuclear Physics B* **1997**, 746-752.

52. Abraham, F. F.; Rudge, W. E.; Plischke, M., Molecular-Dynamics Of Tethered Membranes. *Physical Review Letters* **1989,** *62* (15), 1757-1759.

53. Drovetsky, B. Y.; Chu, J. C.; Mak, C. H., Computer simulations of self-avoiding polymerized membranes. *Journal of Chemical Physics* **1998,** *108* (16), 6554-6557.

54. Abraham, F. F.; Nelson, D. R., Fluctuations In The Flat And Collapsed Phases Of Polymerized Membranes. *Journal De Physique* **1990,** *51* (23), 2653-2672.

55. Schluter, A. D.; Payamyar, P.; Ottinger, H. C., How the World Changes By Going from One- to Two-Dimensional Polymers in Solution. *Macromolecular Rapid Communications* **2016,** *37* (20), 1638-1650.

56. Spector, M. S.; Naranjo, E.; Chiruvolu, S.; Zasadzinski, J. A., Conformations of the Tethered Membrane - Crumpling in Graphitic Oxide. *Physical Review Letters* **1994,** *73* (21), 2867-2870.

57. Dou, X.; Koltonow, A. R.; He, X.; Jang, H. D.; Wang, Q.; Chung, Y.-W.; Huang, J., Self-dispersed crumpled graphene balls in oil for friction and wear reduction. *Proceedings of the National Academy of Sciences of the USA* **2016,** *113* (6), 1528-1533.

58. Onsager, L., The Effects of Shape on the Interaction of Colloidal Particles. *Annals of the New York Academy of Sciences* **1949,** *51* (4), 627-659.

59. Forsyth, P. A.; Marcelja, S.; Mitchell, D. J.; Ninham, B. W., Onsager transition in hard plate fluid. *Journal of the Chemical Society, Faraday Transactions 2* **1977,** *73* (1), 84-88.

60. Harnau, L., Structure and thermodynamics of platelet dispersions. *Molecular Physics* **2008,** *106* (16-18), 1975-2000.

61. van der Kooij, F. M.; Kassapidou, K.; Lekkerkerker, H. N. W., Liquid crystal phase transitions in suspensions of polydisperse plate-like particles. *Nature* **2000,** *406* (6798), 868-871.

62. Hirata, M.; Gotou, T.; Horiuchi, S.; Fujiwara, M.; Ohba, M., Thin-film particles of graphite oxide 1: High-yield synthesis and flexibility of the particles. *Carbon* **2004,** *42* (14), 2929-2937.

63. Watcharotone, S.; Dikin, D. A.; Stankovich, S.; Piner, R.; Jung, I.; Dommett, G. H. B.; Evmenenko, G.; Wu, S. E.; Chen, S. F.; Liu, C. P.; Nguyen, S. T.; Ruoff, R. S., Graphene-silica composite thin films as transparent conductors. *Nano Letters* **2007,** *7* (7), 1888-1892.

64. Worsley, K. A.; Ramesh, P.; Mandal, S. K.; Niyogi, S.; Itkis, M. E.; Haddon, R. C., Soluble graphene derived from graphite fluoride. *Chemical Physics Letters* **2007,** *445* (1-3), 51-56.

65. Cheng, C.; Li, D., Solvated Graphenes: An Emerging Class of Functional Soft Materials. *Advanced Materials* **2013,** *25* (1), 13-30.

66. Hu, J.; Kang, Z.; Li, F.; Huang, X., Graphene with three-dimensional architecture for high performance supercapacitor. *Carbon* **2014,** *67*, 221-229.

67. Guo, F.; Kim, F.; Han, T. H.; Shenoy, V. B.; Huang, J. X.; Hurt, R. H., Hydration-Responsive Folding and Unfolding in Graphene Oxide Liquid Crystal Phases. *ACS Nano* **2011,** *5* (10), 8019-8025.

68. Xu, Z.; Gao, C., Aqueous Liquid Crystals of Graphene Oxide. *ACS Nano* **2011,** *5* (4), 2908-2915.

69. Balankin, A. S.; Matarnoros, D. M.; Leon, E. P.; Rangel, A. H.; Cruz, M. A. M.; Ochoa, D. S., Topological crossovers in the forced folding of self-avoiding matter. *Physica A* **2009,** *388* (9), 1780-1790.

70. Abraham, F. F.; Goulian, M., Diffraction From Polymerized Membranes - Flat vs Crumpled. *Europhysics Letters* **1992,** *19* (4), 293-296.

71. Oh, C.; Sorensen, C. M., Structure factor of diffusion-limited aggregation clusters: Local structure and non-self-similarity. *Physical Review E* **1998,** *57* (1), 784-790.

72. Schmidt, C. F.; Svoboda, K.; Lei, N.; Petsche, I. B.; Berman, L. E.; Safinya, C. R.; Grest, G. S., Existence of a Flat Phase in Red-Cell Membrane Skeletons. *Science* **1993,** *259* (5097), 952-954.

73. Cote, L. J.; Kim, J.; Tung, V. C.; Luo, J. Y.; Kim, F.; Huang, J. X., Graphene oxide as surfactant sheets. *Pure and Applied Chemistry* **2011,** *83* (1), 95-110.

74. Abgrall, P.; Nguyen, N. T., Nanofluidic devices and their applications. *Analytical Chemistry* **2008,** *80* (7), 2326-2341.

75. Rasaiah, J. C.; Garde, S.; Hummer, G., Water in nonpolar confinement: From nanotubes to proteins and beyond. *Annual Review of Physical Chemistry* **2008,** *59*, 713-740.

76. Jiang, Y. N.; Liu, N. N.; Guo, W.; Xia, F.; Jiang, L., Highly-Efficient Gating of Solid-State Nanochannels by DNA Supersandwich Structure Containing ATP Aptamers: A Nanofluidic IMPLICATION Logic Device. *Journal of the American Chemical Society* **2012,** *134* (37), 15395-15401.

77. Han, J.; Craighead, H. G., Separation of long DNA molecules in a microfabricated entropic trap array. *Science* **2000,** *288* (5468), 1026-1029.

78. Wang, Y. C.; Stevens, A. L.; Han, J. Y., Million-fold preconcentration of proteins and peptides by nanofluidic filter. *Analytical Chemistry* **2005,** *77* (14), 4293-4299.

79. Daiguji, H.; Yang, P. D.; Majumdar, A., Ion transport in nanofluidic channels. *Nano Letters* **2004,** *4* (1), 137-142.

80. Pu, Q.; Yun, J.; Temkin, H.; Liu, S., Ion-Enrichment and Ion-Depletion Effect of Nanochannel Structures. *Nano Letters* **2004,** *4* (6), 1099-1103.

81. Stein, D.; Kruithof, M.; Dekker, C., Surface-charge-governed ion transport in nanofluidic channels. *Physical Review Letters* **2004,** *93* (3), 035901.

82. Daiguji, H.; Oka, Y.; Shirono, K., Nanofluidic diode and bipolar transistor. *Nano Letters* **2005,** *5* (11), 2274-2280.

83. Sparreboom, W.; van den Berg, A.; Eijkel, J. C. T., Principles and applications of nanofluidic transport. *Nature Nanotechnology* **2009,** *4* (11), 713-720.

84. Daiguji, H., Ion transport in nanofluidic channels. *Chemical Society Reviews* **2010,** *39* (3), 901-911.

85. Cao, H.; Yu, Z. N.; Wang, J.; Tegenfeldt, J. O.; Austin, R. H.; Chen, E.; Wu, W.; Chou, S. Y., Fabrication of 10 nm enclosed nanofluidic channels. *Applied Physics Letters* **2002,** *81* (1), 174-176.

86. Li, W. L.; Tegenfeldt, J. O.; Chen, L.; Austin, R. H.; Chou, S. Y.; Kohl, P. A.; Krotine, J.; Sturm, J. C., Sacrificial polymers for nanofluidic channels in biological applications. *Nanotechnology* **2003,** *14* (6), 578-583.

87. Kuo, T. C.; Cannon, D. M.; Shannon, M. A.; Bohn, P. W.; Sweedler, J. V., Hybrid three-dimensional nanofluidic/microfluidic devices using molecular gates. *Sensors and Actuators A – Physical* **2003,** *102* (3), 223-233.

88. Eijkel, J. C. T.; Bomer, J.; Tas, N. R.; van den Berg, A., 1-D nanochannels fabricated in polyimide. *Lab On A Chip* **2004,** *4* (3), 161-163.

89. Vlassiouk, I.; Smirnov, S.; Siwy, Z., Nanofluidic ionic diodes. Comparison of analytical and numerical solutions. *ACS Nano* **2008,** *2* (8), 1589-1602.

90. Goldberger, J.; Fan, R.; Yang, P., Inorganic nanotubes: a novel platform for nanofluidics. *Accounts of Chemical Research* **2006,** *39* (4), 239-48.

91. Fan, R.; Huh, S.; Yan, R.; Arnold, J.; Yang, P. D., Gated proton transport in aligned mesoporous silica films. *Nature Materials* **2008,** *7* (4), 303-307.

92. Ali, M.; Yameen, B.; Cervera, J.; Ramirez, P.; Neumann, R.; Ensinger, W.; Knoll, W.; Azzaroni, O., Layer-by-Layer Assembly of Polyelectrolytes into Ionic Current Rectifying Solid-State Nanopores: Insights from Theory and Experiment. *Journal of the American Chemical Society* **2010,** *132* (24), 8338-8348.

93. Israelachvili, J. N., *Surface and Intermolcular Forces*. 3rd ed.; Academic Press: London, UK, **2011**.

94. Nair, R. R.; Wu, H. A.; Jayaram, P. N.; Grigorieva, I. V.; Geim, A. K., Unimpeded Permeation of Water Through Helium-Leak–Tight Graphene-Based Membranes. *Science* **2012,** *335* (6067), 442-444.

95. Kim, H. W.; Yoon, H. W.; Yoon, S.-M.; Yoo, B. M.; Ahn, B. K.; Cho, Y. H.; Shin, H. J.; Yang, H.; Paik, U.; Kwon, S.; Choi, J.-Y.; Park, H. B., Selective Gas Transport Through Few-Layered Graphene and Graphene Oxide Membranes. *Science* **2013,** *342* (6154), 91-95.

96. Li, H.; Song, Z.; Zhang, X.; Huang, Y.; Li, S.; Mao, Y.; Ploehn, H. J.; Bao, Y.; Yu, M., Ultrathin, Molecular-Sieving Graphene Oxide Membranes for Selective Hydrogen Separation. *Science* **2013,** *342* (6154), 95-98.

97. Raidongia, K.; Huang, J., Nanofluidic Ion Transport through Reconstructed Layered Materials. *Journal of the American Chemical Society* **2012,** *134* (40), 16528-16531.

98. Koltonow, A. R.; Huang, J., Two-dimensional nanofluidics. *Science* **2016,** *351* (6280), 1395-1396.

99. Newman, A. C. D., *Chemistry of clays and clay minerals*. Wiley: New York, **1987**.

100. Potts, J. R.; Dreyer, D. R.; Bielawski, C. W.; Ruoff, R. S., Graphene-based polymer nanocomposites. *Polymer* **2011,** *52* (1), 5-25.

101. Walker, G. F., Diffusion of exchangeable cations in vermiculite. *Nature* **1959,** *184*, 1392-1393.

102. Walker, G. F.; Garrett, W. G., Chemical Exfoliation of Vermiculite and the Production of Colloidal Dispersions. *Science* **1967,** *156* (3773), 385-387.

103. Obut, A.; Girgin, I., Hydrogen peroxide exfoliation of vermiculite and phlogopite. *Minerals Engineering* **2002,** *15* (9), 683-687.

104. Agmon, N., The Grotthuss Mechanism. *Chemical Physics Letters* **1995,** *244* (5-6), 456-462.

105. Cukierman, S., Et tu, Grotthuss! and other unfinished stories. *Biochimica Et Biophysica Acta – Bioenergetics* **2006,** *1757* (8), 876-885.

106. Roberts, N. K.; Northey, H. L., Proton and Deuteron Mobility in Normal and Heavy-Water Solutions of Electrolytes. *Journal of the Chemical Society – Faraday Transactions I* **1974,** *70* (2), 253-262.

107. DeCoursey, T. E.; Cherny, V. V., Deuterium isotope effects on permeation and gating of proton channels in rat alveolar epithelium. *Journal of General Physiology* **1997,** *109* (4), 415-434.

108. Knauth, P.; Sgreccia, E.; Donnadio, A.; Casciola, M.; Di Vona, M. L., Water Activity Coefficient and Proton Mobility in Hydrated Acidic Polymers. *Journal of the Electrochemical Society* **2011,** *158* (2), B159-B165.

109. Fan, R.; Huh, S.; Yan, R.; Arnold, J.; Yang, P., Gated proton transport in aligned mesoporous silica films. *Nature Materials* **2008,** *7* (4), 303-307.

110. Yeh, C.-N.; Raidongia, K.; Shao, J.; Yang, Q.-H.; Huang, J., On the origin of the stability of graphene oxide membranes in water. *Nature Chemistry* **2015,** *7* (2), 166-170.

111. Harned, H. S., Owen, B.B., *The Physical Chemistry of Electrolytic Solutions*. Reinhold: **1958**.

112. Kreuer, K. D., On the development of proton conducting polymer membranes for hydrogen and methanol fuel cells. *Journal of Membrane Science* **2001,** *185* (1), 29-39.

113. Longhi, P.; Mussini, P.; Perboni, G.; Rondinini, S., Transference numbers of aqueous HCl up to 15 mol-kg−1 at 25°C: A systematization and reassessment. *Journal of Solution Chemistry* **1995,** *24* (4), 311-324.

114. Tybrandt, K.; Larsson, K. C.; Richter-Dahlfors, A.; Berggren, M., Ion bipolar junction transistors. *Proceedings of the National Academy of Sciences of the USA.* **2010,** *107* (22), 9929-9932.

115. Zhang, J. L.; Yang, H. J.; Shen, G. X.; Cheng, P.; Zhang, J. Y.; Guo, S. W., Reduction of graphene oxide via L-ascorbic acid. *Chemical Communications* **2010,** *46* (7), 1112-1114.

116. Weinstein, J. N.; Leitz, F. B., Electric Power from Differences in Salinity: The Dialytic Battery. *Science* **1976,** *191* (4227), 557-559.

117. Guo, W.; Cheng, C.; Wu, Y.; Jiang, Y.; Gao, J.; Li, D.; Jiang, L., Bio-Inspired Two-Dimensional Nanofluidic Generators Based on a Layered Graphene Hydrogel Membrane. *Advanced Materials* **2013,** *25* (42), 6064-6068.

118. Ji, J. Z.; Kang, Q.; Zhou, Y.; Feng, Y. P.; Chen, X.; Yuan, J. Y.; Guo, W.; Wei, Y.; Jiang, L., Osmotic Power Generation with Positively and Negatively Charged 2D Nanofluidic Membrane Pairs. *Advanced Functional Materials* **2017,** *27* (2), 8.

119. Karnik, R.; Duan, C. H.; Castelino, K.; Daiguji, H.; Majumdar, A., Rectification of ionic current in a nanofluidic diode. *Nano Letters* **2007,** *7* (3), 547-551.

120. Vlassiouk, I.; Siwy, Z. S., Nanofluidic diode. *Nano Letters* **2007,** *7* (3), 552-556.

121. Cheng, L. J.; Guo, L. J., Nanofluidic diodes. *Chemical Society Reviews* **2010,** *39* (3), 923-938.

122. Cheng, L.-J.; Guo, L. J., Ionic Current Rectification, Breakdown, and Switching in Heterogeneous Oxide Nanofluidic Devices. *ACS Nano* **2009,** *3* (3), 575-584.

123. Yan, R.; Liang, W.; Fan, R.; Yang, P., Nanofluidic Diodes Based on Nanotube Heterojunctions. *Nano Letters* **2009,** *9* (11), 3820-3825.

124. Guan, W.; Fan, R.; Reed, M. A., Field-effect reconfigurable nanofluidic ionic diodes. *Nature Communications* **2011,** *2*, 506.

125. Tybrandt, K.; Forchheimer, R.; Berggren, M., Logic gates based on ion transistors. *Nature Communications* **2012,** *3*, 6.

126. Cheng, L.-J.; Guo, L. J., Rectified Ion Transport through Concentration Gradient in Homogeneous Silica Nanochannels. *Nano Letters* **2007,** *7* (10), 3165-3171.

127. Cao, L.; Guo, W.; Wang, Y.; Jiang, L., Concentration-Gradient-Dependent Ion Current Rectification in Charged Conical Nanopores. *Langmuir* **2012,** *28* (4), 2194-2199.

128. Cheng, C.; Jiang, G.; Garvey, C. J.; Wang, Y.; Simon, G. P.; Liu, J. Z.; Li, D., Ion transport in complex layered graphene-based membranes with tuneable interlayer spacing. *Science Advances* **2016,** *2* (2).

129. Huang, J. X., Nanofluidic ion transport through reconstructed layered materials. *Abstracts of Papers of the American Chemical Society*. **2014,** *247*, 1.

130. Yossifon, G.; Mushenheim, P.; Chang, Y.-C.; Chang, H.-C., Nonlinear current-voltage characteristics of nanochannels. *Physical Review E* **2009,** *79* (4), 046305.

131. Yossifon, G.; Chang, Y.-C.; Chang, H.-C., Rectification, Gating Voltage, and Interchannel Communication of Nanoslot Arrays due to Asymmetric Entrance Space Charge Polarization. *Physical Review Letters* **2009,** *103* (15), 154502.

132. Miansari, M.; Friend, J. R.; Banerjee, P.; Majumder, M.; Yeo, L. Y., Graphene-Based Planar Nanofluidic Rectifiers. *The Journal of Physical Chemistry C* **2014,** *118* (38), 21856-21865.

133. Kim, F.; Luo, J.; Cruz-Silva, R.; Cote, L. J.; Sohn, K.; Huang, J., Self-Propagating Domino-like Reactions in Oxidized Graphite. *Advanced Functional Materials* **2010,** *20* (17), 2867-2873.

134. Shao, J.-J.; Raidongia, K.; Koltonow, A. R.; Huang, J., Self-assembled two-dimensional nanofluidic proton channels with high thermal stability. *Nature Communications* **2015,** *6*, 7602.

135. Chianelli, R. R.; Prestridge, E. B.; Pecoraro, T. A.; Deneufville, J. P., Molybdenum disulfide in the poorly crystalline "rag" structure. *Science* **1979,** *203* (4385), 1105-7.

136. Mutz, M.; Bensimon, D.; Brienne, M. J., Wrinkling Transition In Partially Polymerized Vesicles. *Physical Review Letters* **1991,** *67* (7), 923-926.

137. Gornyi, I. V.; Kachorovskii, V. Y.; Mirlin, A. D., Rippling and crumpling in disordered free-standing graphene. *Physical Review B* **2015,** *92* (15), 22.

138. Weir, M. P.; Johnson, D. W.; Boothroyd, S. C.; Savage, R. C.; Thompson, R. L.; Parnell, S. R.; Parnell, A. J.; King, S. M.; Rogers, S. E.; Coleman, K. S.; Clarke, N., Extrinsic Wrinkling and Single Exfoliated Sheets of Graphene Oxide in Polymer Composites. *Chemistry of Materials* **2016,** *28* (6), 1698-1704.

139. Poulin, P.; Jalili, R.; Neri, W.; Nallet, F.; Divoux, T.; Colin, A.; Aboutalebi, S. H.; Wallace, G.; Zakri, C., Superflexibility of graphene oxide. *Proceedings of the National Academy of Sciences of the USA* **2016,** *113* (40), 11088-11093.

140. Sofos, M.; Goldberger, J.; Stone, D. A.; Allen, J. E.; Ma, Q.; Herman, D. J.; Tsai, W.-W.; Lauhon, L. J.; Stupp, S. I., A synergistic assembly of nanoscale lamellar photoconductor hybrids. *Nature Materials* **2009,** *8* (1), 68-75.

141. Herman, D. J.; Goldberger, J. E.; Chao, S.; Martin, D. T.; Stupp, S. I., Orienting Periodic Organic−Inorganic Nanoscale Domains Through One-Step Electrodeposition. *ACS Nano* **2011,** *5* (1), 565-573.